BRIGHT PbS NANOSHEETS THROUGH ORGANIC AND INORGANIC SURFACE PASSIVATION

Megh Raj Khadka

A Thesis

Submitted to the Graduate College of Bowling Green
State University in partial fulfillment of
the requirements for the degree of

MASTER OF SCIENCE

December 2023

Committee:

Liangfeng Sun, Committee Chair

Marco Nardone

Alexey Zayak

ABSTRACT

Liangfeng Sun, Committee Chair

Over the past several decades, nanomaterials have undergone significant improvements and developments. Among these, infrared nanomaterials have potential applications in fiber optics communications, night vision, and sensing, with PbS nanomaterials standing out as a particularly promising option.

In this work, we explored two distinct techniques to enhance the light-emitting efficiency of PbS nanosheets: organic ligand passivation and inorganic shell encapsulation. For the organic surface passivation, we utilized tributylphosphine as a ligand. Meanwhile, for inorganic passivation, we designed a core/shell structure using $PbCl_2$. To achieve this inorganic core/shell structure, we pioneered a robust synthesis method capable of producing orange nanoplatelets. Notable, both strategies led to a substantial increase in the photoluminescence quantum yield. Such nanosheets with augmented quantum yield could be pivotal in the evolution of photonic devices, encompassing light-emitting diodes, solar cells, and lasers.

To my beloved father

ACKNOWLEDGMENTS

I wish to express my deepest appreciation to my advisor, Dr. Liangfeng Sun. I am immensely grateful for the opportunity he provided me to work under his guidance. His continuous support, and valuable recommendations have been pivotal to my academic and research progress. I also owe a great deal to the members of our research group. I would like to extend my gratitude to Dr. Yiteng Tang, whose assistance and insightful suggestions have been invaluable throughout my research journey. I extend my thanks to the Department of Physics and Astronomy at Bowling Green State University for their generous financial support which enabled me to pursue my studies. I also appreciate the advice and dedication of all the committee members who devoted their time to guide me in this project. To my family, especially my wife, I am deeply grateful for the unwavering encouragement and support throughout my academic journey. Your belief in me has been my beacon of motivation. This work was made possible by the support from the National Science Foundation under the grant no. [1905217]. Additionally, I wish to acknowledge the aid of AI tools and my group members in refining my writing. Lastly, I wish to dedicate this work to my beloved father, Tikaram Khadka. This accomplishment is not just mine, but a fulfillment of one of his dreams. His memory continues to inspire and guide me, and I am proud to honor him with this achievement.

TABLE OF CONTENTS

Page

LIST OF FIGURES

LIST OF TABLES

CHAPTER 1. INTRODUCTION

1.1 Introduction of nanomaterial

In 1959, renowned physicist Richard Feynman spoke about the concept of nanotechnology and its potential for synthesis through the direct manipulation of atoms in his talk “There’s Plenty of Room at the Bottom”[1]. From that point forward, terms such as nanotechnology, nanomaterials, and so on became common parlance as the field developed. In a simple sentence, nanotechnology involves the manipulation of matter within the range of 1 to 100 nanometers (nm) where at least 1 dimension of the material is sized in that range [2].

In recent years, there has been a surge of interest in these materials due to their extraordinary mechanical, electrical, optical, and magnetic properties. Nanomaterials are used in many different fields of scientific study, as well as in more commercial applications, such as cosmetic, agriculture, sports, solar cells, and manufacturing.

1.2 Excitons

When a material absorbs photons with energy higher than its band gap, the electrons in the valence band (VB) of the material are excited and move to the higher energy conduction band (CB). This process creates positively charged holes in the VB as the electrons leave as shown in figure 1.1. The interaction between holes and electrons in semiconductors occurs through the Coulomb force, which leads to the formation of excitons. This Coulombic interaction between the positively charged holes and negatively charged electrons plays a crucial role in the binding of excitons and their behavior within the semiconductor materials [3] .

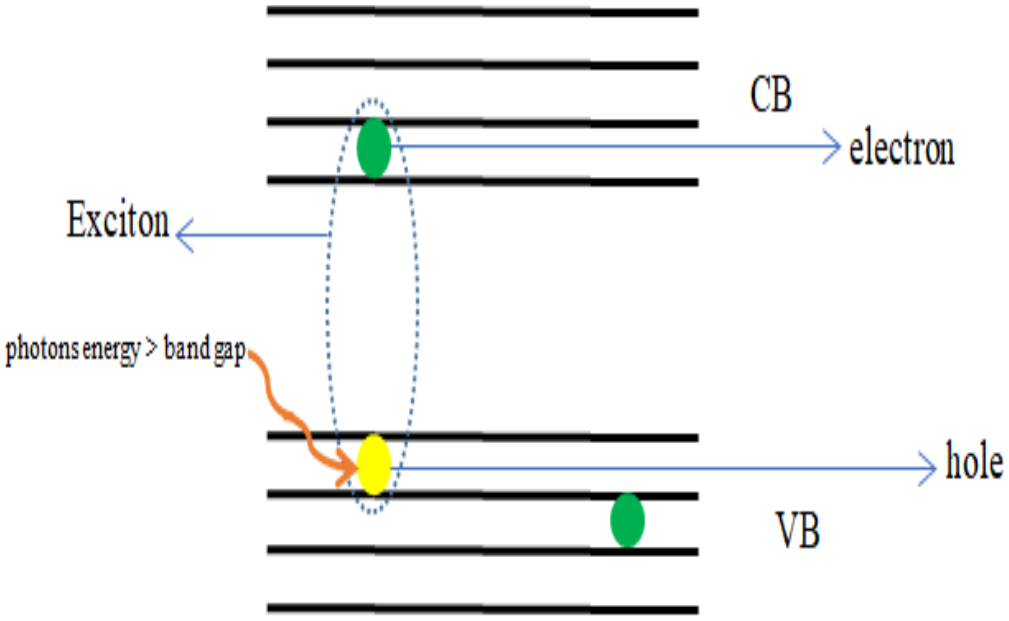

Figure 1.1: Formation of exciton in semiconductor.

The distance of separation between this electron in CB and the hole in VB is the Bohr radius. These excitons are electrically neutral quasi-particles, which means they act like the hydrogen atom. Similarly, excitons are classified into two types (a) Frenkel excitons, and (b) Mott-Wannier excitons. In materials with a relatively low dielectric constant, the Coulomb interaction between an electron and a hole can be strong, resulting in small-sized excitons that are comparable in size to the unit cell of the material. These types of excitons, known as Frenkel excitons, are commonly observed in crystals like alkali halides and organic molecular crystals composed of aromatic molecules such as anthracence and tetrances. In semiconductors, the dielectric constant is generally large. Consequently, this tends to reduce the Coulomb interaction between electrons and holes, which has a radius larger than the lattice spacing. Wannier-Mott

excitons are typically found in semiconductor crystals with small energy gaps and high dielectric constant but have also been identified in liquids, such as liquid xenon [4] .

When the particle approaches the nanoscale, motion of electrons is confined such that continuous energy state become discrete. This effect, known as quantum confinement, increase or widen the band gap. Hence, as the size decreases quantum confinement increases.

The radius of exciton Bohr can be calculated from the following formula [4].

$$a_b^* = \varepsilon_r \left(\frac{m}{\mu}\right) a_b$$

Where, ε_r= relative permittivity

m = mass of electron

μ = effective reduced mass

a_b= Bohr radius (~0.053 nm)

Table 1 is the exciton Bohr radius of some materials [5].

Table 1: Bohr radius of some semiconductors

Material	Bohr radius (nm)
CuCl	1
CdSe	6
PbS	20
InAs	34
PbSe	46
InSb	54
PbTe	46

When the diameter of any given material is reduced beyond that of their Bohr radius, it becomes a nanomaterial. As the diameter continues to shrink new properties will emerge, one of which being quantum confinement. Quantum confinement effects refer to the behavior of electrons within nanoscale particles, where their energy levels, potential wells, valence bands, conduction bands, and energy band gaps are described. These effects occur as the size of the particle shrinks beyond that of the wavelength of an electron. The confinement of electrons and holes within nanocrystals is greatly influenced by the material properties, particularly the Bohr radius. For example, the exciton Bohr radius of PbS is 20 nm, if the size is reduced beyond this point, then quantum confinement on that side is seen, and PbS will show a broader band gap than its bulk materials.

1.3 Types of nanomaterials

Nanomaterials can be divided into three distinct types, based on their structure and the nature of the quantum confinement in each type. These are quantum dots, nanorods, and nanosheets. When PbS nano-dots have a diameter smaller than 20 nm, the excitons experience confinement in all three dimensions (3D), resulting in a wider energy gap. Similarly, if a nanorod is created with a diameter below 20 nm, it will exhibit 2D confinement along its diameter in two directions. Likewise, when a nanosheet is formed with a thickness below 20 nm, the confinement occurs in 1D along the height only. Figure 1.2 illustrates the density of states for various dimensional nanomaterials [6] and their potential shapes, providing a visual reference to identify where quantum confinement can occur. Hence, we can state that band gap decreases with the decrease in the order of quantum confinement.

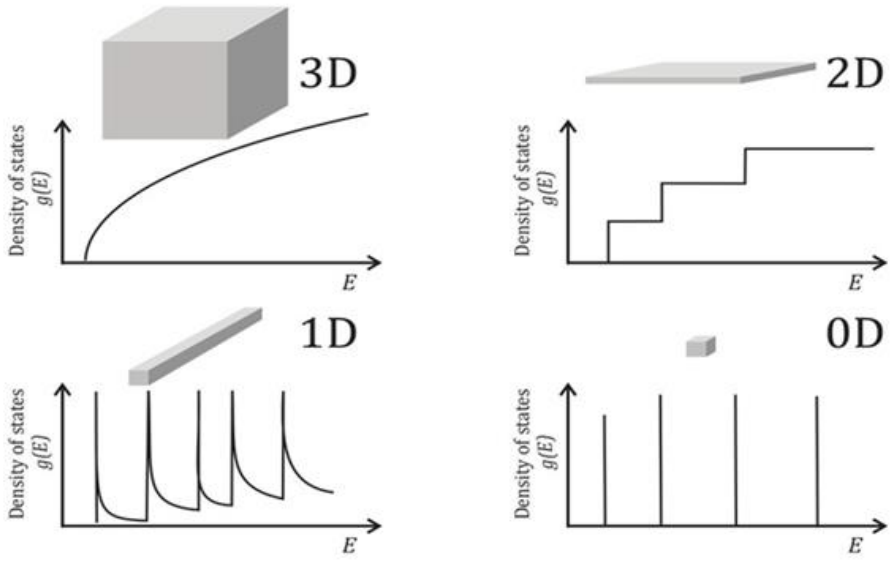

Figure 1.2: Density of states for various dimensions of nanomaterials.

1.4 Relation between band gap and size of nanomaterials

The band gap between a semiconductor material in its bulk form differs from that of its nanostructure. In nanostructure, the band gap increases as quantum confinement is intensified or as the size of the nanomaterial decreases [7] . Quantum dots, for instance, utilize the highest occupied molecular orbital (HOMO) level and the lowest unoccupied molecular orbitals (LUMO) level to represent their energy levels. The HOMO level corresponds to the valance band maximum in a semiconductor, while the LUMO level defines the conduction band minimum. The difference in the LUMO and HOMO levels defines the energy gap of the quantum dot. Figure 1.3 [7] illustrates the relationship between the size of PbS quantum dots and their corresponding energy gap.

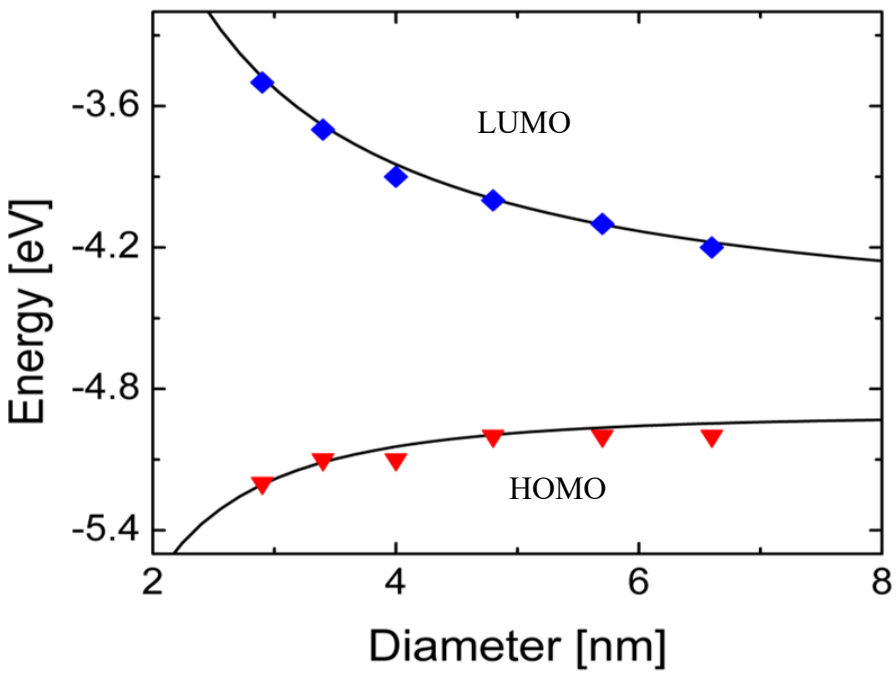

Figure 1.3: Size dependent energy gap of the PbS quantum dot.

1.5 Objective of this project

The principal objective of my research is to amplify the quantum yield of PbS nanosheets and nanoplatelets. Nanomaterials with high quantum yield bear extensive applications, and their progression can considerably influence a diverse array of scientific and technology sectors. When it comes to PbS materials emitting in the IR range (1100 nm–1600 nm emission spectrum), elevating their quantum yield becomes increasingly crucial. These materials serve as potent optical reporters in molecular imaging and sensing and are essential in telecommunication technology. Additionally, they are integral components in the development of electro-optical and photovoltaic devices [8] [9].

The colloidal PbS nanosheets have garnered significant attention for their potential applications in optoelectronics and photonic devices [10] . These nanosheets offer the advantages of tunable electronic band structure with varying thickness, along with high carrier mobility and efficient carrier multiplication [11] . Compared to quantum dot films, nanosheets exhibit larger carrier mobility due to the absence of charge-carrier scattering at the boundaries of quantum dots [12] [13] . This feature is particularly valuable in optoelectronic devices that require high current density. Additionally, the synthesis of 2D nanosheets not only overcomes this obstacle but also maintains quantum confinement in 1D as shown in figure 1.4 [14] .

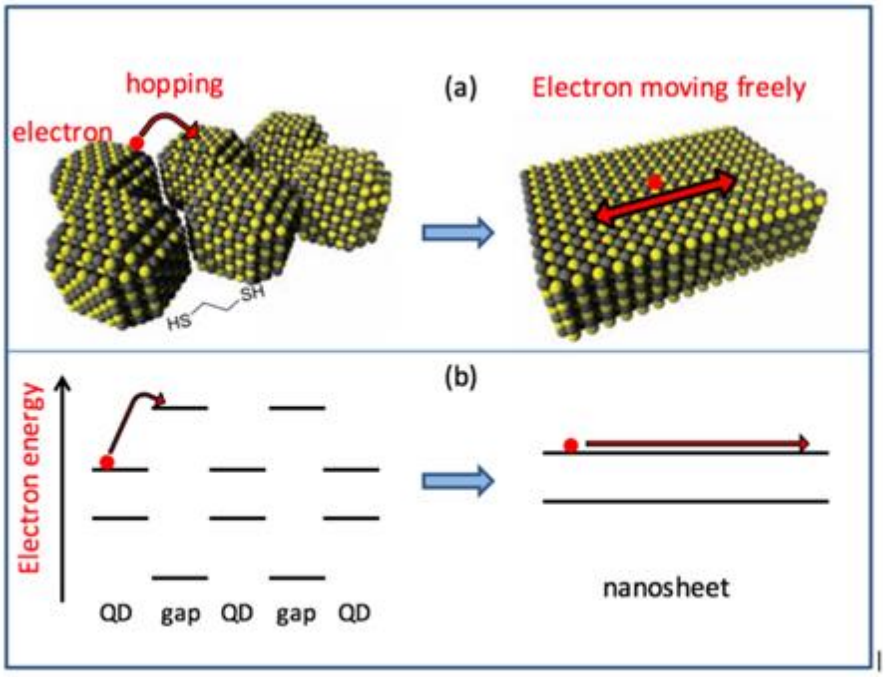

Figure 1.4: Charge mobility in quantum dot and nanosheets

However, when it comes to applications that demand high light-emitting efficiency, larger lateral sizes of nanosheets are unfavorable. This is because larger nanosheets possess more surface states, and their high carrier mobility contributes to charge trapping in these states, resulting in low photoluminescence quantum efficiency for PbS nanosheets [15] . One solution to improve their optical properties is to reduce the lateral size of the nanosheets to approximately the Bohr radius of the exciton in PbS [16].By doing so, the surface states can be significantly reduced while still primarily maintaining 1D confinement. This leads to enhanced light-emitting efficiency and preserves unique properties associated with anisotropic confinement, including improved optical absorption and reduces Auger recombination [17] [18] [19] . Another solution is to passivate the surface through an organic or inorganic reagent, which helps to improve the photoluminescence quantum yield.

Hence, to know the application of PbS nanosheets and nanoplatelets in optoelectronic devices, we need to know its photoluminescence, photoluminescence lifetime, photoluminescence quantum yield, and its structure, which are covered in this project.

CHAPTER 2. EXPERIMENTAL METHOD- SYNTHESIS

In this chapter we will discuss the method we adopted to synthesize various types of PbS nanomaterials.

2.1 Synthesis of nanomaterials

In the realm of nanoscience, the synthesis of nanomaterials is widely regarded as a creative and cost-effective endeavor. Two well-known approaches for the synthesis of nanomaterials are:

2.1.1 Bottom-up approach

This approach involves the assembly of nanomaterials from smaller building blocks, such as atoms, molecules, or nanoparticles. Through controlled growth processes, these building blocks are combined and organized to form the desired nanoscale structure. Examples of bottom-up synthesis methods include chemical vapor deposition, sol-gel synthesis, and molecular self-assembly. Bottom-up synthesis allows for precise control over the size and shape of the resulting nanomaterials [20] [21] [22].

2.1.2 Top-down approach

In contrast to the bottom-up approach, the top-down approach involves the reduction of larger bulk materials to obtain nanoscale structures. This method typically involves processes such as mechanical milling, lithography, or etching, where the starting material is gradually reduced in

size to reach the desired nanoscale dimensions. This approach is often criticized due to its numerous flaws, including various defects and a lack of precise control over size and shape [23] [24].

In our research, we have employed a bottom-up approach known as colloidal synthesis method. This method involves preparing two precursors solutions in separate flasks, which are then mixed under carefully controlled synthesis conditions. One of the advantages of this method is that we have significant control over various parameters, such as pressure, temperature, and time. This ease of control makes the colloidal synthesis method user friendly and highly productive in terms of desired outcomes.

2.2 Experimental setup

All syntheses were conducted under an air-free nitrogen environment using a standard Schlenk line system. The primary purpose of the Schlenk line system is to ensure strict air free conditions by either creating a vacuum or supplying nitrogen/argon gas. This system, also referred to as a vacuum gas manifold, is composed of two separate manifolds with multiple ports.

One manifold is connected to a nitrogen or argon gas supply, which is further connected to an oil bubbler to release excess pressure from the nitrogen supply. The other manifold is linked to a high- pressure vacuum system that effectively removes organic vapors and gaseous reaction products. To prevent contamination of the vacuum system by these organic vapors, a liquid nitrogen cold trap is employed.

The ports of both manifolds are interconnected via a stopcock, which enables the delivery of either nitrogen gas or vacuum to the connected tube as desired by the user. When the stopcock

is opened in the direction of the nitrogen gas, it supplies nitrogen to the tube and ultimately to the connected flask. Conversely, when the stopcock is opened towards the vacuum, it provides a vacuum to the system.

The entire Schlenk line system is operated within a fume hood to ensure safety. Figure 2.1 [25] depicts the schematic diagram of the Schlenk line system for better visualization.

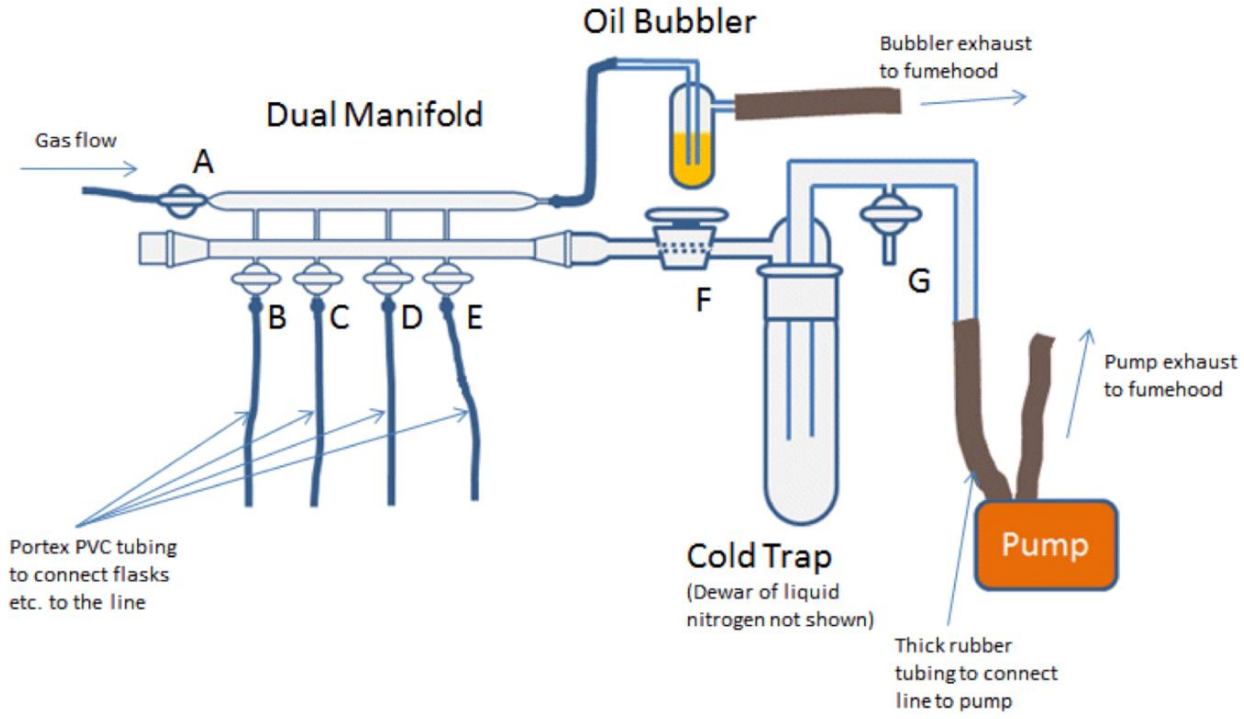

Figure 2.1: Schematic diagram of standard Schlenk line system.

2.3 Synthesis of PbS nanosheets

The synthesis method used for the production for PbS nanosheets is based on the procedure developed by the Wise group [25] and further improved [26]. The process involved the preparation of the lead precursor by dissolving 0.506 gm of lead oxide (PbO) 99.999% pure in a mixture of 1.8 ml of oleic acid (OA) and 10 ml of diphenylether (DPE) within a 3-neck flask. The entire setup was maintained in a nitrogen environment to eliminate air. The solution was then heated to 100°C and subjected to degassing for 20 minutes using a vacuum system. This step facilitated the conversion of lead oxide to lead oleate, and the removal of acetic acid. After degassing, the lead precursor was once again placed in a nitrogen environment.

In a separate 3-neck flask, the sulfur precursor was prepared by adding 0.012 gm of thioacetamide (TAA) to 70 ml of N, N-dimethylformamide under a nitrogen atmosphere. Subsequently, 930 ml of Trioctylphosphine (TOP) was added to the flask after replacing the air with nitrogen to prevent the formation of TOPO, which occurs due to the oxidation of TOP. Then the solution was allowed to equilibrate at room temperature for approximately an hour.

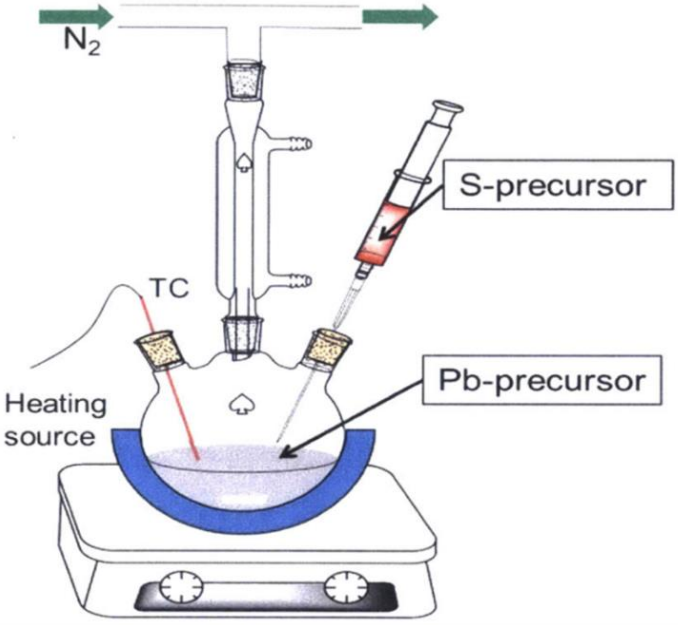

http://hdl.handle.net/1721.1/98741

Figure 2.2: An experimental setup using Schlenk line system for synthesis of PbS nanosheets.

Upon preparing both precursors, the temperature of the lead precursor was raised to 130° C, which is 20°C above the boiling point of the chloroalkane used. The sulfur precursor was then introduced into the lead precursor solution, and the mixture was stirred for approximately 5 minutes to facilitate the growth of 2D PbS nanosheets. Subsequently, the final solution was allowed to cool down slowly to room temperature over several hours. This gradual cooling process is important for the stabilization and formation of the desired nanosheet structure.

To purify the reaction mixture, centrifugation was employed for 5 minutes at a speed of 3000 rpm. This step helps to separate the nanosheets from the surrounding solution. The resulting pellet was subjected to washing and subsequent centrifugation using toluene for several cycles. Each wash helps remove impurities and further purify the nanosheets. Finally, the

purified nanosheet precipitation was dispersed in either toluene or tetrachloroethylene. These solvents provide a suitable medium for the storage and subsequent characterization of the PbS nanosheets.

2.4 Synthesis of PbS nanoribbons

The synthesis method for colloidal PbS nanoribbons is an adaptation of a previous procedure [25]. The process begins by preparing the lead precursor inside a 3-neck flask. Lead oxide (0.506 gm is dissolved in diphenyl ether (10 ml and oleic acid (1.8 ml. It is crucial to maintain an inert atmosphere in the flask, free from any nitrogen flow. The mixture is then subjected to degassing at a higher vacuum for twenty minutes at 100°C, resulting in a pale yellow-colored lead precursor.

Next, a chloroalkane (1 ml, such as 1,1,2-trichloroethane (TCA or chloroform, is added to the flask at a temperature 4°C below its boiling point. Simultaneously, the sulfur precursor is prepared separately by dissolving thioacetamide (0.012 gm in N,N-dimethylformamide (70 µl and trioctylphosphine (930 µl under a nitrogen environment.

Once both precursors are ready, the temperature of the lead precursor is set to the desired level, ranging from 70°C to 170°C. The sulfur precursor is then injected into the flask while the reaction solution is continuously stirred. The reaction time is adjusted based on the selected reaction temperature.

After a few minutes of reaction, the solution is slowly cooled down to room temperature. The final solution is washed twice with toluene to remove impurities and subjected to centrifugation to precipitate the nanoribbons. The resulting nanoribbons are then redispersed into toluene for further use or characterization.

2.5 Synthesis of PbSCl nanoplatelets

This is a new technique for synthesizing colloidal PbSCl nanoplatelets. The process involves combining 0.457 gm of 99% pure lead oxide (PbO with 1.62 ml of oleic acid (OA and 27.9 µl of Oleylamine (OLA in a three-neck flask. Additionally, 10 ml of diphenyl ether and 0.0378 gm of 99.99% pure $PbCl_2$ are added to the mixture. The purpose of adding OLA is to dissolve $PbCl_2$. the three-neck flask is then heated to 110°C for one hour under a continuous flow of nitrogen. After an hour, the solution becomes clear, and the temperature is reduced to 100°C. Once stable at 100°C, over degassing is performed by opening an additional valve for 20 minutes and at that moment temperature further reduce to around 76°C. Once degassing is complete, the temperature of the mixture is raised to 130°C.

On the other hand, we prepare the sulfur precursor by dissolving 0.012 gm of thioacetamide in 70 µl of N,N-dimethylformamide and 930 µl of trioctylphosphine in a nitrogen environment. The mixture is left to mix for one hour. Once the lead precursor is ready, confirmed by its stable reaction temperature of 130°C, the sulfur precursor is injected into the lead precursor using an injection method. The reaction is allowed to proceed for 20 minutes. It's worth noting that both the reaction temperature and time are crucial factors that control the thickness of the nanoplatelets. After the 20-minutes reaction period, the heat supply is deactivated, and the solution is allowed to cool slowly until it reaches room temperature. The final solution is then subjected to two washes with toluene to remove any impurities present. Following the washing step, centrifugation is performed to separate and collect the nanoplatelets. The resulting nanoplatelets are then dispersed again in toluene for subsequent utilization or characterization.

2.6 Synthesis of PbS quantum dots

The synthesis of PbS quantum dots was carried out using a modified version of the Hines methods [27]. In a typical synthesis, 0.22 gm of PbO was mixed with 0.64 ml of Oleic acid (OA and 9.96 ml of 1-Octadecene (ODE in a 3-neck flask. The flask was heated in a nitrogen environment, and the temperature was set to 150°C. The mixture was allowed to dissolve for an hour.

For the sulfur precursor, 126 µl of TMS was combined with 6 ml of ODE in another 3-neck flask. The mixture was stirred for 30 minutes or more to ensure proper dissolution. Next, the temperature of the lead precursor was adjusted from 150°C to 90°C. Once the temperature stabilized at 90°C, the sulfur precursor was injected using a 5 ml syringe. The reaction was allowed to proceed for approximately 1.5 minutes. After the reaction time, the flask was transferred to an ice-water bath to rapidly cool down the solution. The cooling process was conducted under a nitrogen environment until the solution reached room temperature. Then, the final solution is subjected to a purification process. The solution is washed twice using a mixture of butanol and methanol. After the washing process, the solution is then centrifuged to precipitate the PbS quantum dots. Centrifugation separates the quantum dots from the liquid phase, allowing for their collection as a pellet.

CHAPTER 3.EXPERIMENTAL METHOD-CHARACTERIZATION

In this chapter, we briefly discuss the characterization methods we adopted in our lab.

3.1 Transmission Electron Microscopy (TEM)

To examine the morphology of the synthesized sample, transmission electron microscopy (TEM) was employed as a powerful characterization technique. TEM utilizes a beam of electrons that passes through the sample, interacting with its structure and generating an image. This technique is particularly useful for confirming our sample, whether it is nanosheet, or nanoribbons, or nanoplatelets, or quantum dots.

To perform TEM imaging, specially functionalized copper grids were utilized. A small drop of the synthesized sample, diluted in toluene, was drop-casted onto a TEM grid. The grid with the sample was then allowed to dry for several minutes, ensuring the sample adheres to the grid surface. A representative TEM image of the nanoplatelets is depicted in figure 3.1. This image provides valuable insights into the morphology and structure of the synthesized nanoplatelets.

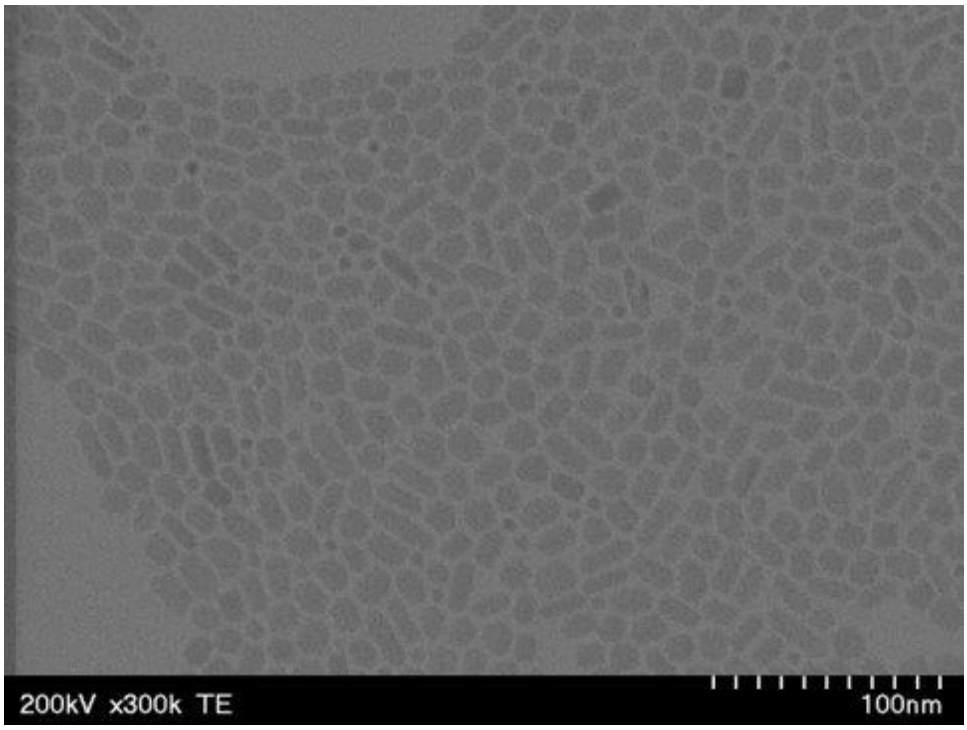

Figure 3.1: TEM image of PbSCl nanoplatelets synthesis at 130^0C for 20 minutes.

3.2 X-Ray diffraction

X-ray diffraction (XRD) is a crucial technique for determining various properties of materials, including the average spacing between atomic layers or rows, crystal orientation, crystal structure, and size of nanomaterials. In our laboratory, we employ the Bruker D8 ADVANCE XRD machine, which utilizes a high voltage power supply to generate X-ray diffraction patterns from the sample. It involves directing an X-rays beam onto a sample and analyzing the resulting scattering pattern. The X-rays interact with the crystal lattice of the nanosheet, causing constructive and destructive interference. This interference pattern contains information about the arrangement of atoms in the material. A detector positioned opposite the sample collects the diffracted X-rays, and the data is used to generate a diffraction pattern.

For XRD analysis, first we took the sample, dried it, and added chloroform, and drop cast it on the glass slide, make it thick and wait for it to be completely dried. Then put in the

XRD machine, to collect the diffraction data. The collected XRD data from PbS nanoplatelets, quantum dots, nanosheets, and nanoribbons to analyze their crystal structure and thickness for each facet. Figure 3.2 depicts the XRD machine currently utilized in our laboratory.

To measure the thickness of our nanoparticles, we use Scherrer equation [28]

$$Thickenss\ (L) = \frac{K\lambda}{\beta cos\theta};$$

Where,

L = thickness

K = Scherrer constant which is equal to 1

λ = X-ray wavelength (0.15418 nm)

β = FWHM in radian

θ is Bragg angle

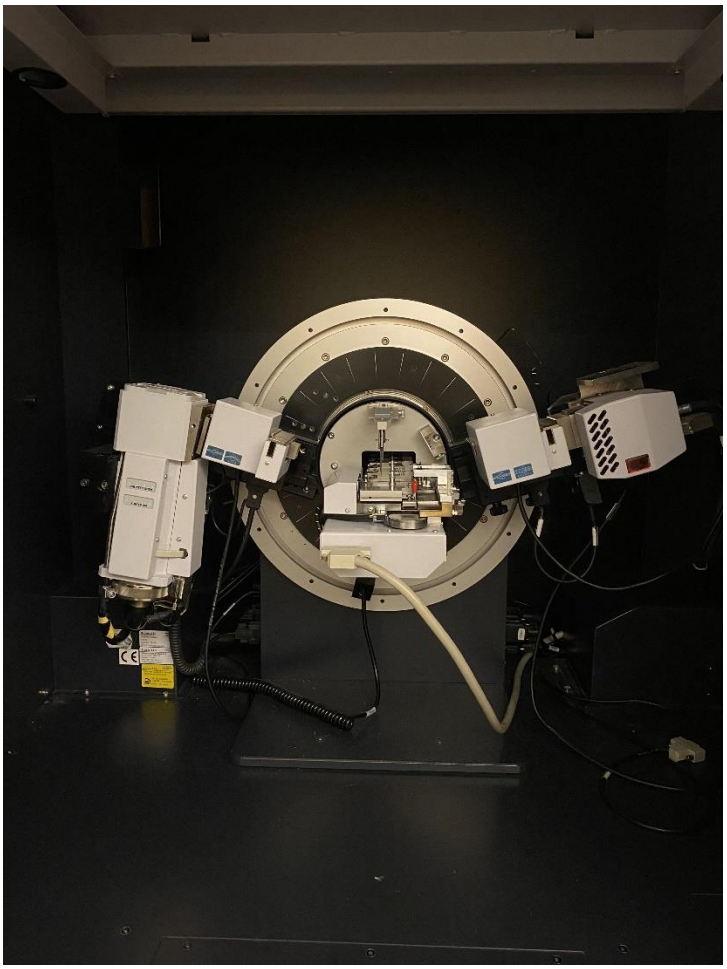

Figure 3.2: XRD machine used in our lab.

In the above figure left-hand side rectangular box is for incident X-ray, which passes through the sample kept at the holder, and then the detraction signal is collected by the right-hand side detector, and then the software compline the data and gives us the graph.

3.3 Photoluminescence spectroscopy

Photoluminescence (PL) spectroscopy is a technique used to measure the light emitted from a material after the absorption of photons. When a sample absorbs photons, both photoluminescence and Raman scattering can occur. However, PL is generally more prominent compared to the phonon vibrations associated with Raman scattering. PL

encompasses both fluorescence and phosphorescence processes and is a result of the absorption or emission processes between different energy levels within the material. It provides valuable information about the energy band structure, electronic transitions, and optical properties of the material. The figure 3.3 represents a schematic representation of photoluminescence [29], illustrating the process of absorptions, and optical properties of the material.

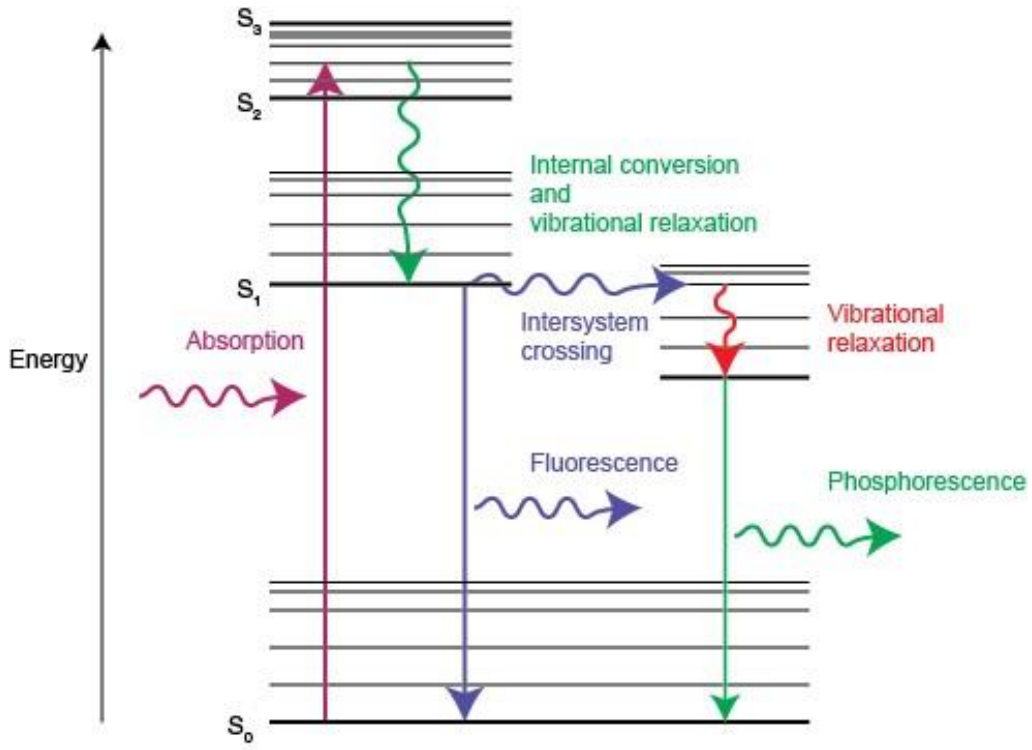

Figure 3.3: Schematic representation of Fluorescence and Phosphorescence

For the measurement of PL of the sample, a home-built spectrometer was utilized. The spectrometer setup consisted of an Argon laser, a monochromator, and an infrared (IR) detector. To align the laser beam onto the specimen, two mirrors and two irises were employed. To control the laser signal, a chopper was utilized to pulse the continuous laser beam. Additionally, a filter was employed to regulate the laser intensity. Two convex mirrors were used to combine the emitted light from the specimen. A bandpass filter was also included before the detector to block specific wavelengths.

The detector signals were then directed to a lock-in amplifier and subsequently transmitted to a computer, where they were converted into digital data. The measurements were controlled using software programmed in LabView. The PL system schematic diagram can be found in the figure 3.4 [30][31] accurate measurement and analysis of the emitted PL signal.

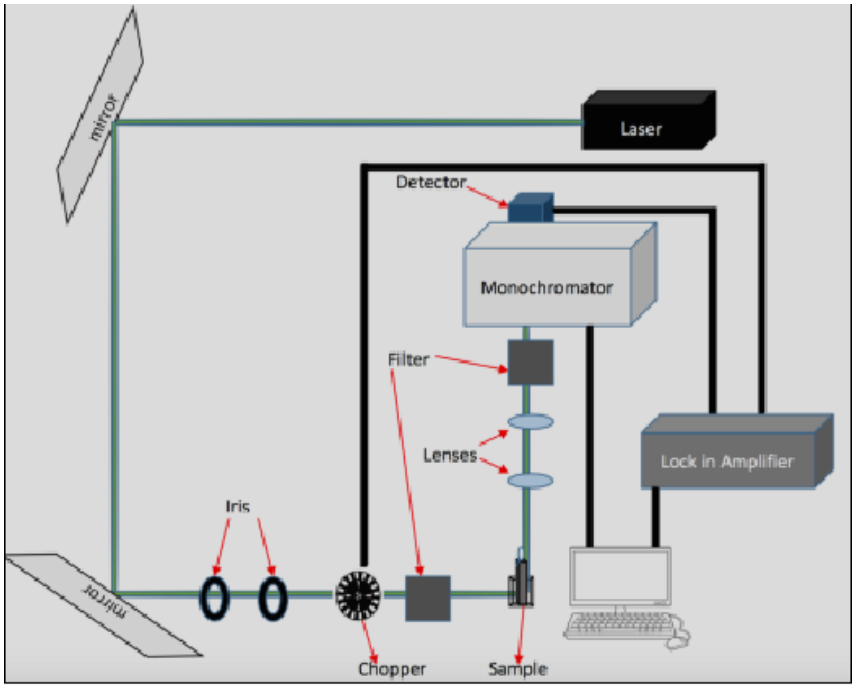

Figure 3.4: Schematic diagram for home-built Photoluminescence Spectroscopy

3.4 Optical absorption measurement

In semiconductor nanocrystals, the electrons absorb the energy of incident photons, and the extent of absorption varies depending on the material and synthesis conditions. The absorption spectra differ between different materials, such as nanosheets and nanoribbons. To measure the absorption spectra of the specimen, a home-built system was employed. Commercial instruments often face challenges in accurately measuring the absorption spectra of nanosheets due to the strong scattering of light from their lateral dimensions. However, in this case, an integrating sphere was utilized to diffuse the scattering light and direct it to the spectrometer, as depicted in figure 3.5 below. This approach is based on a method utilized by Friend and his co-workers for calculating the photoluminescence quantum yield of thin films [32]. By employing the integrating sphere, the scattered light is effectively captured towards the spectrometer for precise measurement of the absorption spectra.

To calculate the absorption of light, Beer-Lambert law is used [33].

$$A = \log\left(\frac{I_0}{I}\right)$$

Where,

A = absorption of light at a particular wavelength

I_0= Intensity of the light without any sample

I = Intensity of light after passing through the sample

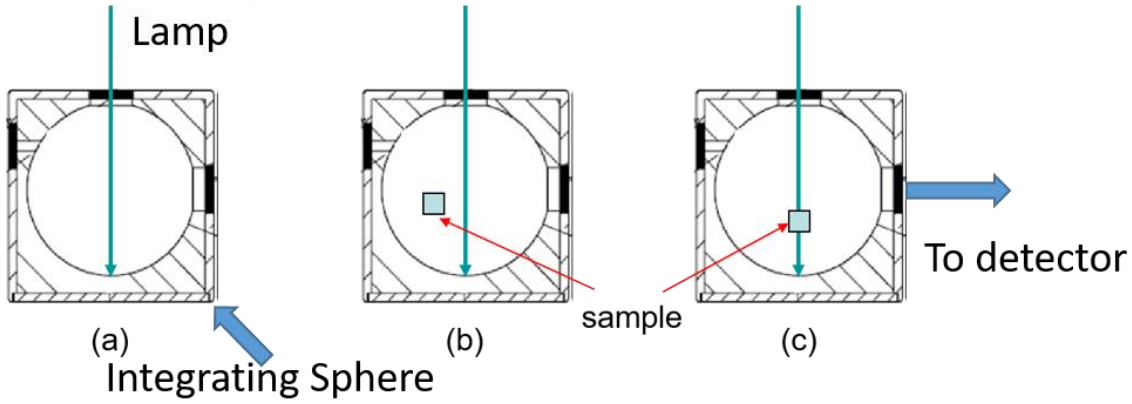

Figure 3.5: Absorption measurement techniques using integrating sphere to diffuse the scattering light a) light inside the integrating sphere without the sample, b) with the sample but at off position, and c) on position that is light hitting the sample inside the integrating sphere.

3.5 Photoluminescence lifetime measurement

When a specimen absorbs photons, the electrons transition to an excited state. Subsequently, these excited electrons return to the ground state by emitting photons. The average time it takes for the electron to return to the ground state after photon absorption is referred to as the photoluminescence lifetime. Photoluminescence lifetime spectroscopy is a technique utilized to investigate the decay of photoluminescence over time. It involves studying the temporal behavior of the emitted light as the excited electrons transition back to the ground state. The decay process from the excited state to the ground state can often be described by a single exponential decay, which can be calculated as [34] [30] [31],

$$I(t) = I_0 e^{\left(-\frac{t}{\tau}\right)}$$

Where, I_0 = Intensity of electron at time t = 0

I(t) = intensity of electron at time t

τ = decay time

Mostly for nanosheets photoluminescence decay is biexponential rather than single exponential decay, which can be calculated as

$$f(t) = A_1 \cdot e^{\left(\frac{-t}{\tau_1}\right)} + A_2 \cdot e^{\left(\frac{-t}{\tau_2}\right)}$$

Where, $\tau_1$and τ_2 are the decay time, and A_1 and A_2 are the pre-exponential factor to represent the fraction of fluorophores with respective lifetime.

The lifetime is determined in the given equation by the time it takes for the initially excited population to decrease by a factor of 1/e or 37%. The advantage of utilizing photoluminescence (PL) lifetime measurement is that it remains unaffected even when the concentration of the sample is altered. To measure the PL lifetime at t = 0, the sample is stimulated by a brief pulse of light from a light source. As the pulse is generated, a time digitizer starts counting and stops as soon as the emitted photon reaches the detector. This time interval between the two signals is then plotted against the intensity of the emitted photon to calculate the lifetime. The collected data was plotted on a logarithmic scale, and a single exponential or double exponential fitting method was employed using Origin Pro software to determine the lifetime. In our experiment setup, we employed an incident IR pulse laser with a wavelength of 1064 nm or a green laser with a wavelength of 532 nm to excite the sample. To generate the 532 nm green laser, we utilize a process known as a second harmonic generator. The second harmonic of the 1064 nm picosecond IR laser was produced by employing a KTP crystal. This

crystal has the property of doubling the frequency of the incident pulse laser light when passing through it [35]. As a result, the 1064 nm IR laser light was converted into a 532 nm green laser through this process. For our measurements, when the emission of the sample fell below 1200 nm, we typically opted to use the green laser for excitation and lifetime measurements. This choice was likely made because the green laser's wavelength falls within a suitable range for efficient excitation and measurement of the sample's lifetime in such cases.

3.6 Absolute quantum-yield measurement

The fluorescence quantum yield is defined as the ratio of the number of photons emitted to the number of photons absorbed [36]

$$Quantum\ Yield\ = \frac{photons\ emitted}{photons\ absorbed}$$

To calculate the photoluminescence quantum yield, we followed the procedure outlined by Friend and his colleagues [32]utilized to achieve isotropic redistribution of light throughout the sphere's interior surface. The excitation beam is generated by passing light from a quartz-tungsten halogen lamp (Oriel 66187) through a narrow slit and a lens, resulting in a rectangular light spot on the cuvette containing the sample. Two color-glass filters are positioned before the entrance of the integrating sphere to limit the excitation wavelength within the range of 850 nm to 1000 nm. The light exciting the integrating sphere is collected by two lenses and directed to a spectrometer (Action SP-2357, Princeton Instrument). A femtowatt photoreceiver (Model 2153, New Focus Inc.) is installed on the spectrometer's exit side to measure the light power at the specified wavelength. The excitation beam is periodically interrupted by a fan, and a lock-in amplifier is employed to suppress background noise during measurements. The spectral response of the entire system is calibrated using a quartz-tungsten halogen lamp (20W

QTH, Newport). The sample is placed in a small glass cuvette and mounted on a sample holder, allowing the sample to either intercept or bypass the excitation light beam. Three spectra are captured: a) excitation light beam only, b) sample in the integrating sphere without the excitation light beam, and c) sample in the excitation light beam as shown in figure 3.5 above. In each photon number spectrum (intensity x wavelength versus wavelength), five parameters are calculated: (area under the excitation light spectrum) $L_a,\ L_b,\ L_c$ (area under the PL spectrum), where subscript a, b, and c correspond to the $P_b,\ and\ P_c$. The quantum yield is subsequently determined using the following equation [32].

$$\eta = \frac{(L_b \cdot P_c) - (L_c \cdot P_l)}{L_a(L_b - L_c)}$$

CHAPTER 4. BRIGHT PbS NANOSHEET WITH ORGANIC SURFACE PASSIVATION

The efficiency of colloidal quantum dots is often limited by poor charge transport, which originates from multiple trapping sites provided by quantum dots surface defects [37]. These defect states act as trapping centers for photogenerated charges, reducing their charge mobility and enhancing recombination, thus setting a limit to the cell thickness and light absorption efficiency [38]. To address this issue, the concentration and depth of surface traps are controlled by managing the ligands surrounding the quantum dots and passivating their surfaces at the atomic level [38] [39]. Surface passivation can be achieved using various organic ligands or epitaxial overcoating with a wide-bandgap semiconductor, enabling efficient radiative recombination of charge carriers. Photoluminescence quantum efficiency approaching unity have been achieved, indicating effective suppression of non-radiative recombination pathways using these strategies [16]. However, attempts to use a range of organic ligands for surface passivation result in a relatively structureless absorption spectrum, even for extremely narrow size distributions. This behavior has been attributed to incomplete passivation of the surface interactions with both charge carriers, resulting in one charge carrier strongly interacting with the surface, thus promoting charge spectrum [40]. The surface of semiconductors nanoparticle often contains electronically active states due to unsaturated surface bonds or dangling bond states. Surface passivation aims to rebind these dangling bonds with a passivating agent while maintaining the neutrality of the whole system. A good surface passivation will remove localized surface states from the band gap but will not change the intrinsic behavior of the HOMO and LUMO.

In many experiments, trioctylphosphine (TOP) is used to passivate nanoparticles [41] since the presence of TOP ligands on CdSe quantum dot surfaces leads to better photoluminescence efficiency [42]. For CdSe quantum dots, TOP typically binds to the surface Se sites but not the surface Cd sites, and TOPO is shown to bind strongly to the surface of Cd atoms only [42]. Researchers, such as Sargent and his co-workers, have found that improving the passivation of any surface defects associates with dangling bonds is important due to unpassivation sulfur surface anions [17]. Indeed, we utilize tributylphosphine (TBP) to passivate the sulfur surface anions. The main reason for using TBP over TOP is due to its short hydrocarbon chain, as a long hydrocarbon chain can greatly hinder charge transport between nanocrystals [43] [44].

4.1 Transmission Electron Microscope (TEM) images

Transmission electron microscopy (TEM and scanning electron microscopy (SEM are employed to verify the shape and size of the nanoparticles. Based on the images below, it is evident the sample corresponds to PbS nanoribbons. The synthesis of these PbS nanoribbons took place for a duration of 4 hours at a reaction temperature of 70°C.

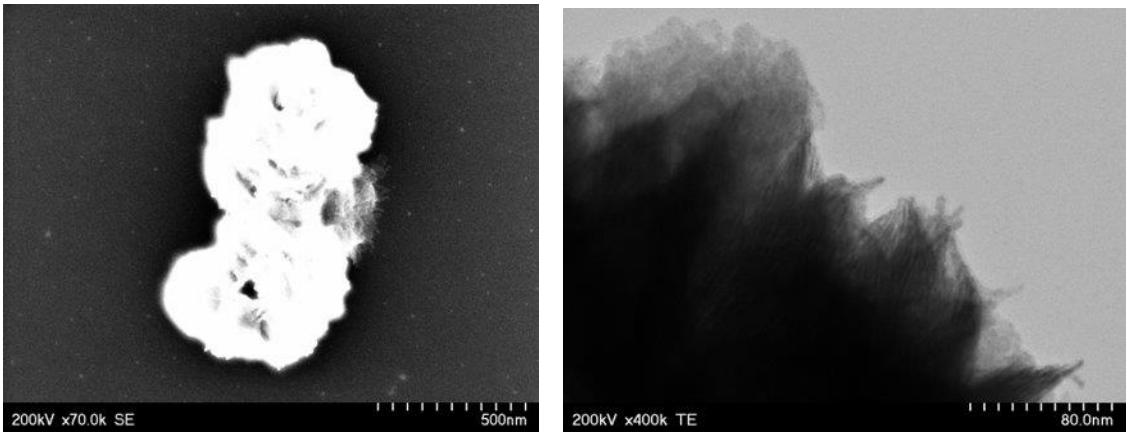

Figure 4.1: Right and Left images are the Scanning electron microscopy and TEM of PbS nanoribbons prepared at 70°C respectively.

4.2 Photoluminescence (PL) measurement

First, the PbS nanoribbons were surface passivated using TBP. The process involved taking 2 ml of PbS nanoribbons and placing them in a glass vial. The nanoribbons were then dried using a nitrogen stream. Once the nanoribbons were dried, 0.2 ml of TBP was added to the vial in a nitrogen environment. The solution was kept in a glass vial to allow the passivation process to occur, and measurements were taken at various time intervals to monitor the progress of passivation.

Before passivating the PbS nanoribbons, the synthesis was conducted at 70°C with a reaction time of 4 hours. The photoluminescence (PL) peak was observed at 1296 nm, with a full width half maximum (FWHM) of 217.9 nm, determined through a perfect Gaussian fit in Origin Pro. After the passivation process, samples were taken in cuvette, and the initial PL measurement was recorded as 0 hours. The PL peak exhibited a slight blue shift, indicating a shift towards shorter wavelengths, with a new peak observed at 1284 nm (a 12 nm blue shift). This blue shift could be attributed to the etching of the surface layer by TBP during the passivation process.

Moreover, the FWHM decreased from 217.9 nm to 193.98 nm at 0 hours after surface passivation. This reduction in FWHM suggests that the nanosheets might have been non-uniform initially, after adding TBP, the thicker parts of the nanosheets were removed, resulting in a more uniform structure. This phenomenon is clearly visible in the PL diagram below.

However, after 30 hours, no PL was detected, and the solution became clear. This observation might indicate that the surface passivation process occurred rapidly and the TBP caused the lead in the PbS nanoribbons to be pulled out, leading to the destruction of the structure.

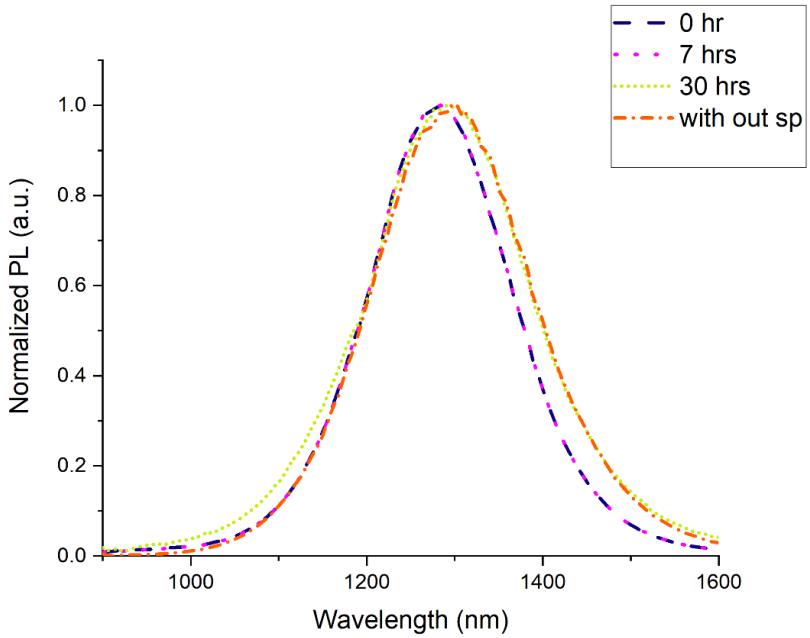

Figure 4.2: PL spectrum of PbS nanoribbon measured at various time; the orange line with short dash-dot represents the PL without surface passivation, while the blue, magenta, and green lines with dash, dot, and short dash respectively represent the PL after treatment with TBP recorded at 0, 7, and 30 hours respectively.

4.3 Absolute PL quantum-yield measurement

To assess the brightness of PbS nanosheets, we utilized the method of absolute photoluminescence (PL) quantum yield measurement. The figure 4.3 displays the spectra of the lamp, a sample in the on position, and a sample in the off position. Our measurements focused on determining the PL quantum yield, a measure of how efficiently the nanosheets emit light upon excitation.

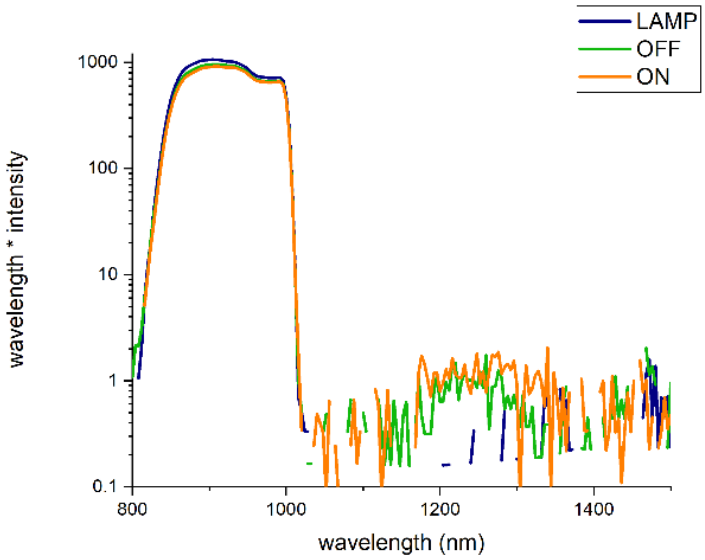

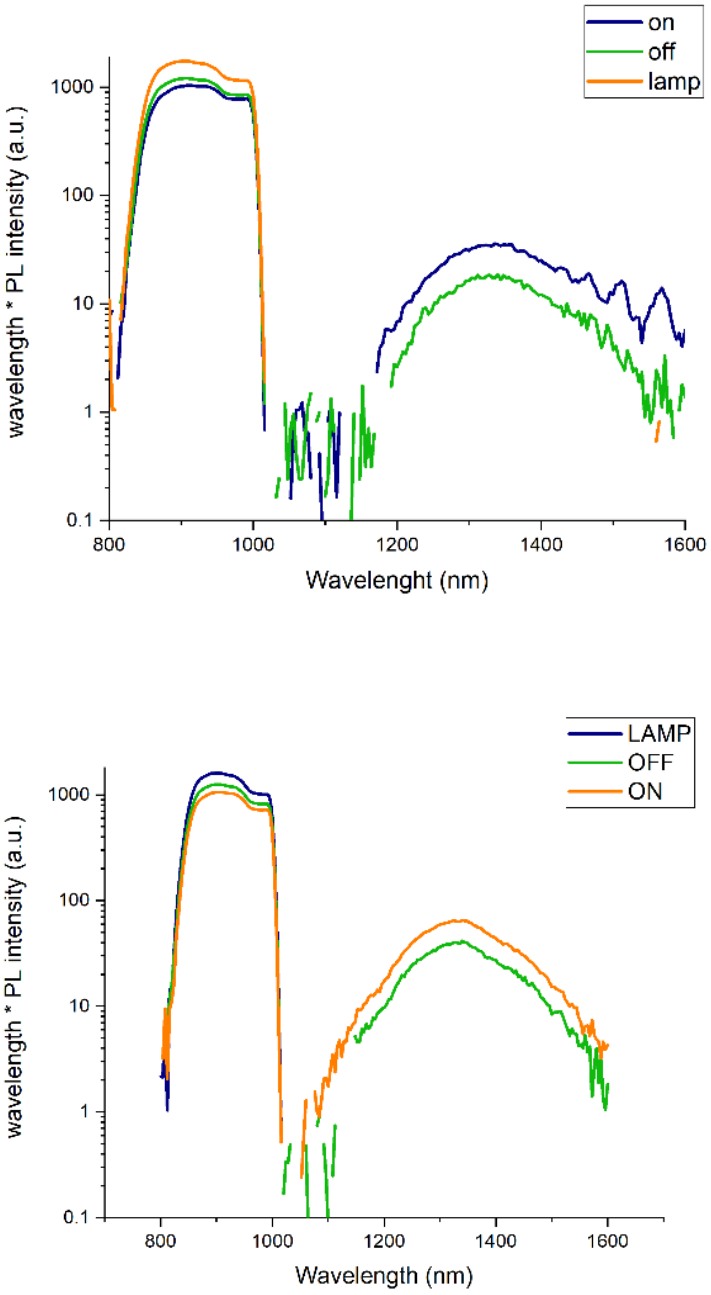

Figure 4.3: Experimental graph obtained by absolute quantum yield measurement of PbS nanoribbon a) without surface passivation. b) after treated with TBP 0 hours c) 30 hours

The analysis of the above figures clearly indicates a significant increase in quantum yield, even shortly after the treatment with TBP. The quantum yield rises from 4.5% to 16.4% representing a more than double increment in the efficiency of light emission. Additionally, the nanoribbons display further increases in PL quantum yield after TBP treatment, reaching a remarkable 31.26% within a short time span of 30 hours. However, beyond this time, the quantum yield begins to decrease, eventually leading to a fading of the PL signal, as mentioned in their earlier PL section.

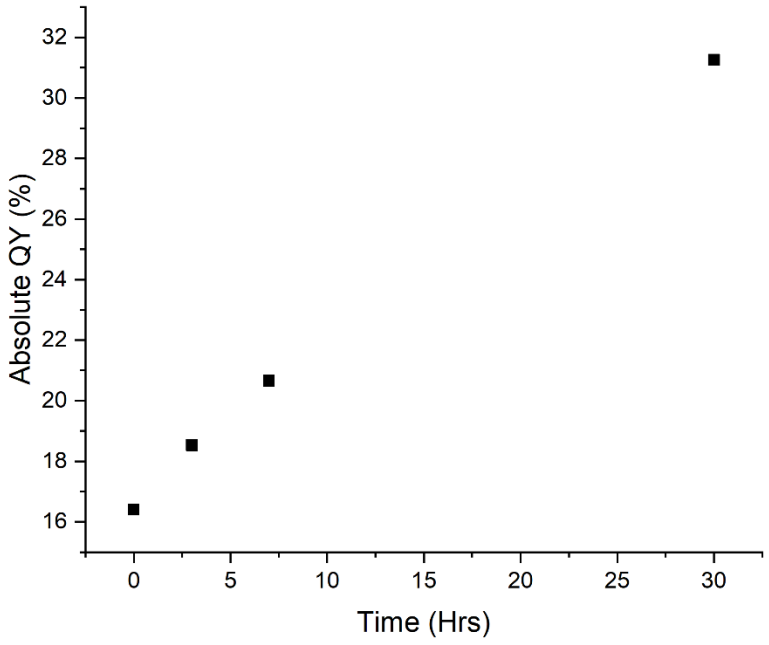

Figure 4.4: Absolute PL quantum yield Vs time of PbS nanoribbon after treated with TBP.

This enhancement in optical properties is attributed to the reduction of surface states. Surface atoms often possess dangling bonds that can form in-gaps states and trap charges,

consequently quenching the PL. The introduction of TBP leads to the formation of chemical bonds with these surface atoms, effectively reducing the number of surface trap states. This reduction in surface traps allows for improved light emission, leading to the observed increase in the quantum yield.

4.4 Time-Resolved Photoluminescence decay (TPL)

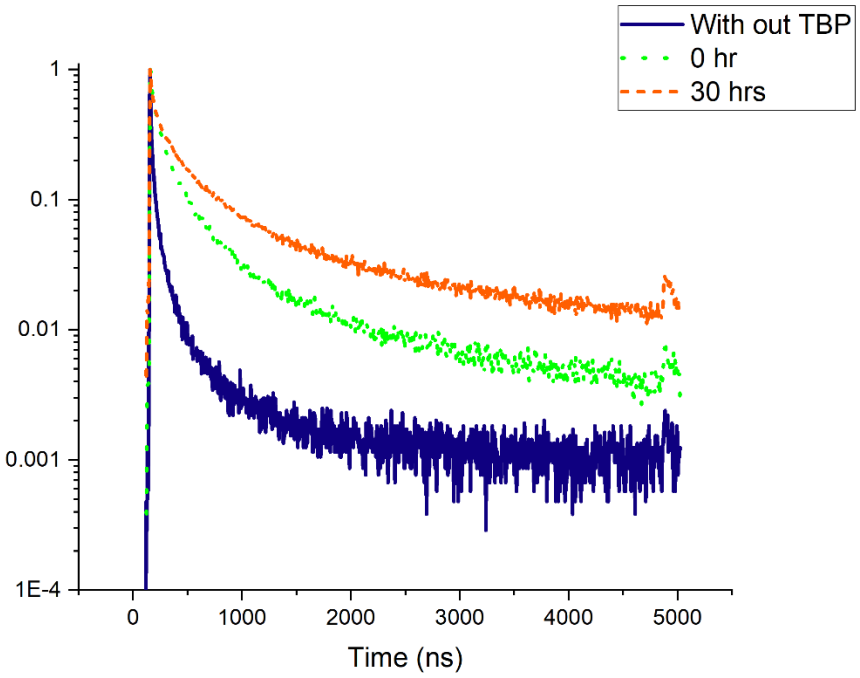

Figure 4.5: Time-dependent photoluminescence of PbS nanoribbons at 1292 nm after treated with TBP at various time.

The time-resolved photoluminescence (PL) decay analysis of PbS reveals a double exponential decay behavior. As evident from the data, the lifetime of the PL signal increases with an increase in the time of surface passivation using TBP. This observed increase in lifetime can be attributed to the surface passivation process, wherein TBP likely covers the bare sulfur

atoms on the surface of the nanoribbons. As a result, the number of surface trap sites and defects is reduced, leading to a decrease in non-radiative recombination processes and enhancing the overall lifetime of the PL signal. After performing double exponential decay fitting using Origin Pro, the two-time constants (τ_1 and τ_2) were determined. Without treating TBP, the value was found to be 28.88 ns and 11.82 ns, respectively. However, after 30 hours of surface passivation with TBP, these time constants increased significantly to 42.32 ns and 426.50 ns respectively.

These results further validate that the surface passivation using TBP is effective in improving the optical properties of the PbS nanoribbons, as evidenced by the increase in PL lifetime. The reduction in surface trap sites and defects due to TBP treatment leads to a substantial increase in the radiative recombination rate, resulting in longer lifetime of the photoluminescence signal.

4.5 Conclusions

In this study, we investigated the optical properties of PbS nanoribbons before and after surface passivation with TBP. The experiments focused on a nanoribbon synthesis performed at 70°C with the reaction time of 4 hours. We recorded the photoluminescence (PL), absolute quantum yield, and PL decay measurement for each state of the experiment and reached the following conclusions.

- After passivation with TBP, we observed a slight shift in the PL signal. This shift may be attributed to the TBP's etching effect on the surface of the nanoribbons.
- Additionally, we noticed a decrease in the full width at half-maximum (FWHM) of the PL spectra after passivation. This reduction could be due to the uniformity created by TBP on the nanosheets, resulting in thicker and more consistent parts of the nanoribbons.

- The introduction of TBP during the passivation process led to a notable reduction in surface trap states. This reduction resulted in an enhancement of the quantum yield, allowing us to achieve a high quantum yield in a shorter period.
- Interestingly, during the measurement period, lead from the PbS nanoribbons were pulled out, which became evident after 30 hours of measurement. As a result, the solution became clear.

In summary, surface passivation with TBP showed promising results in improving the optical properties of PbS nanoribbons. The slight shift in PL, decreased FWHM, reduced surface trap states, and increase in quantum yield demonstrate the potential of TBP passivation for enhancing the performance of these nanoribbons. However, further experiments and characterization with different synthesis conditions and longer-term studies would be beneficial to fully understand and optimize these effects.

4.6 Future work

In this project, we comprehensively investigated the optical properties of PbS nanoribbons synthesized at 70°C for 4 hours, both before and after surface passivation with TBP, using TCA as the solvent. Our study encompassed various aspects of the nanoribbon's behavior, including PL, QY, PL decay, and changes in surface trap states. Building on these findings, our future experiments aim to develop deeper into the effects of nanoribbons and nanosheets thickness variations. We intend to explore how different thickness influences the optical properties of these materials and how surface passivation with TBP can enhance their performance further. Moreover, we plan to investigate the impact of using different solvents, such as hexane, toluene, and chloroform, during the surface passivation processes. Each solvent

may introduce unique characteristics to the nanoribbons and nanosheets, potentially affecting their optical behavior.

CHAPTER 5. BRIGHT PbS NANOSHEET WITH INORGANIC $PbCl_2$ CORE/SHELL

In the field of colloidal nanocrystals (NCs), two-dimensional (2D) nanoplatelets (NPLs) have emerges as a novel class of nanocrystals that exhibit characteristics similar to epitaxial quantum wells while retaining the advantages of being suitable for solution-based processing [45]. Various research groups have demonstrated that 2D NPLs hold great promise for innovative photonic applications, including single particle electronic devices [46], color-saturated light-emitting diodes with narrow electroluminescence spectra [47], luminescence-based oxygen sensors [48], and low-threshold lasers [49]. These NPLs combine strong confinement in one direction, enabling tunable optical properties through the NPL thickness, with weakly bound exciton motion in the other two dimensions, resulting in an enhanced band-edge oscillator strength [49]. Shape control of colloidal NCs towards 2D NPLs results in unique spectroscopic properties, such a short photoluminescence (PL lifetime [50], high color purity [47], reduced Stokes shift [51], exceptionally large exciton and biexciton binding energies [52] [53], and suppressed Auger recombination [54]. While most of the explored 2D nanostructures have focused on materials with energy gaps in the visible spectrum including nanoplatelets [55] [54] [56] and 2D perovskites [57], and there is less exploration in the infrared region. Infrared materials, like PbS with an energy gap of 0.4 eV at room temperature, have significant potential applications in fiber optical communications, sensing, and infrared photonic devices. The tunable energy gap of 2D PbS, ranging from 0.4 eV to 1 eV depending on thickness, corresponds to wavelengths of absorbed or emitted light from 1.2 microns to 3.1 microns, covering the entire fiber optical communication band (1.23 to 1.68 microns [58].

The growth mechanism of PbS nanosheets has been confirmed as a 2D attachment of PbS quantum dots by Ghadendra and co-worker [59]. Shashini and co-workers demonstrated the negative effect of acetic acid on the synthesis, and they provided robust method using lead oxide for achieving 100% successful synthesis [26]. PbS nanoribbons were synthesized by changing the degassing conditions [16]. Despite the belief that PbS nanosheets have less exposed sulfur on their surface, the as-synthesized PbS nanosheets exhibit a low photoluminescence quantum yield, usually lower than 6% [16]. The introduction of short ligands during the synthesis may help in passivating the surface. Additionally, the use of excess lead chloride can lead to improved surface passivation. Enhance air stability and a high photoluminescence quantum yield of PbS quantum dots were achieved by Weidman et al using lead chloride as the lead precursor [60]. Further studies by Sarah et al demonstrated the presence of a Pb_xCl_y shell surrounding the normal PbS quantum dots, resulting in PbS/Pb_xCl_y nanocrystals with a smaller Stokes shift, indicating better surface passivation by the shell [61]. The excess lead chloride may also form a perovskite-like shell with a PbS core, as confirmed by NMR studies by Philippe et al [62]. This lead chloride-based nanocrystals show a potential application in luminescence due to their stability and narrow size distribution [63].

In our experiment, we present a novel method for synthesizing PbSCl nanoplatelets. Building on previous work in our lab, where we demonstrated the oriented attachment of PbS nanosheets by PbS quantum dots using chloroalkane as a co-solvent [16] [26] [59], this study showcases that chloride ions can also induce a two-dimensional attachment of PbS quantum dots, leading to the formation of nanoplatelets. Notably, these nanoplatelets exhibit a bright photoluminescence quantum yield, indicating their potential for various optoelectronic applications.

5.1 Transmission Electron Microscopy (TEM) images

To determine the structure, shape, and size of 2-dimensional nanoparticles, we employed transmission electron microscopy (TEM imagining techniques. The TEM images below represent PbS/$PbCl_2$ core/shell nanoplatelets. The images validate that our innovative synthesis method produces nanoplatelets of satisfactory morphology. The sample shown corresponds to nanoplatelets synthesized at 130^0C with a reaction time of 20 minutes. The lower image represents the analogous sample preserved in toluene.

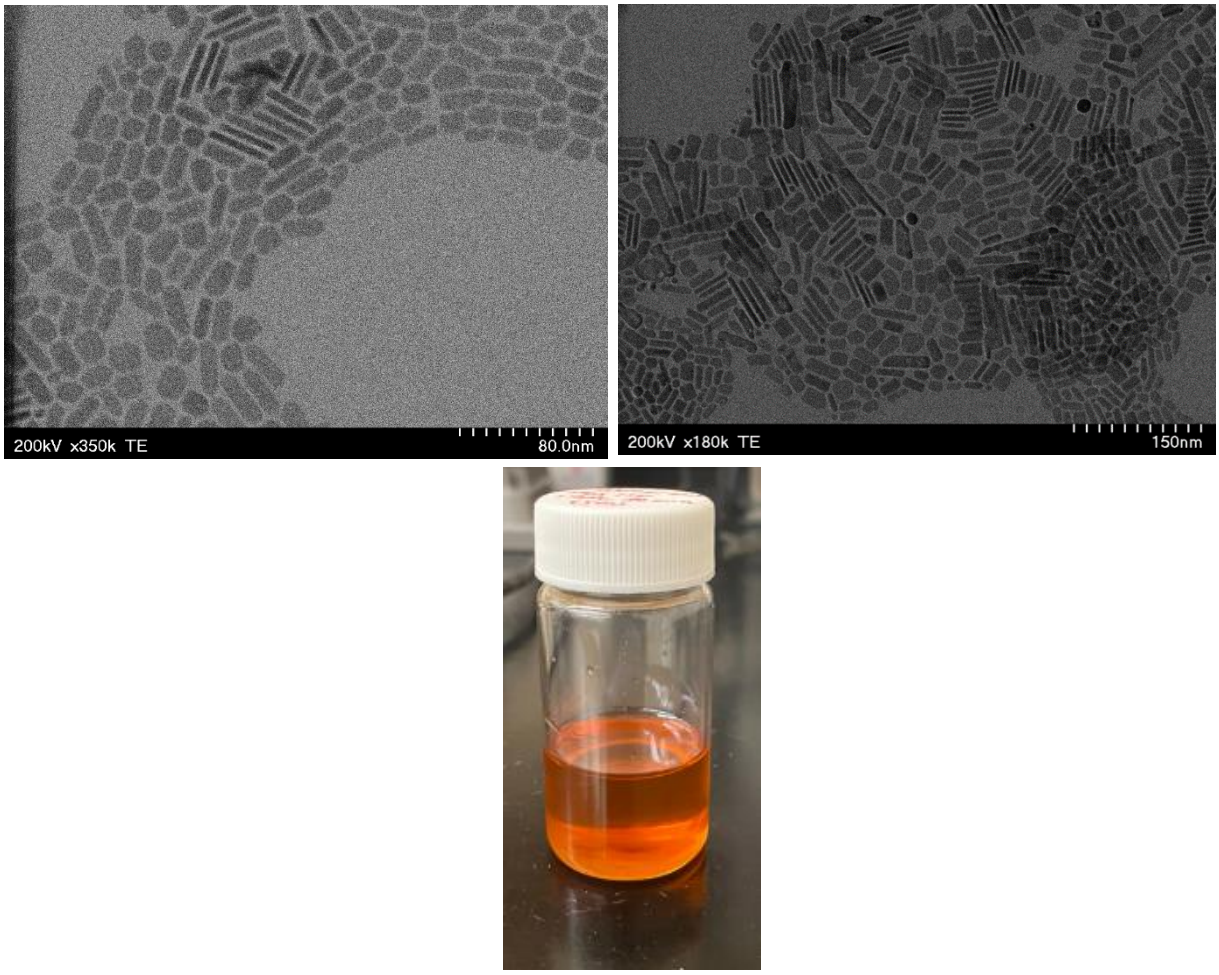

Figure 5.1: The top both are TEM images of PbSCl nanoplatelets synthesis at 130°C for 20 minutes and the bottom is its corresponding sample stored in toluene.

5.2 Photoluminescence (PL) measurement

In our lab, we use 445 nm of blue continuous laser for the excitation and record the emission with the help of the IR femto detector. Our detector can detect up to 1675 nm wavelength, as my nanoparticle's complete spectrum of PL needs to go beyond our range. To

solve this problem, we can best fit our Gaussian curve and find all the required data like full-width half maximum.

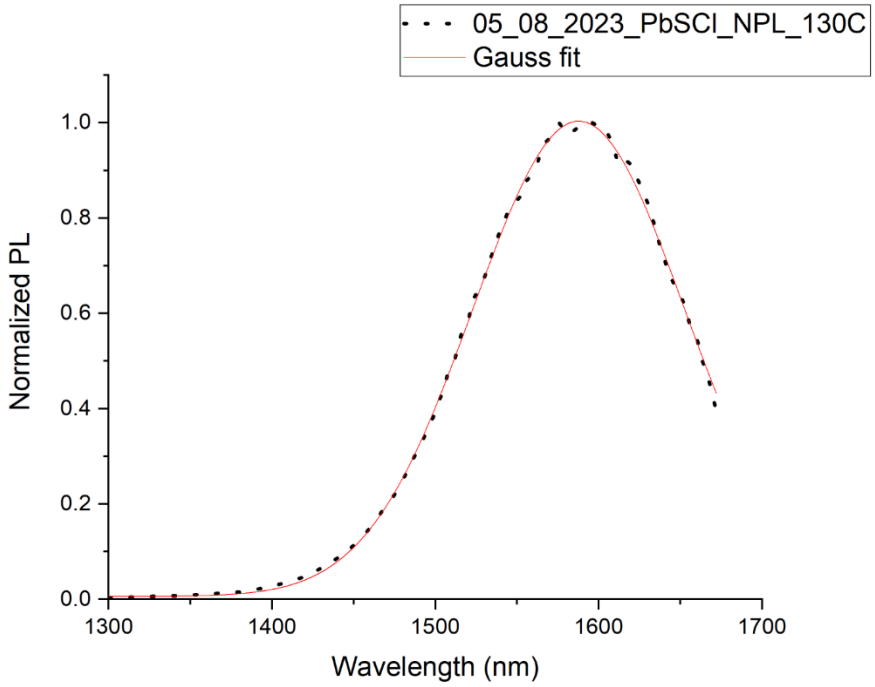

Figure 5.2: Photoluminescence of PbSCl nanoplatelets, the dotted line is from sample and red line is fitted curve done by origin.

When the PbSCl nanoplatelets were excited by a blue continuous laser, it emits radiation which was detected by IR Femto detectors. The PL spectra show a spectral at 1587 nm, and the full width at half maximum was 152.195 nm which was obtained after Gauss fit as in the red curve above. The fitting was done with Origin Pro. The intensity of the peak was so high that we needed to attenuate the incident beam 10 times. The PL peak depends on the reaction temperature and time. If we go on reducing the temperature the peak shows a blue shift. The reaction time also plays a role in shifting PL peak, as we go on increasing time, it will show a red

shift but not significantly as compared to reaction temperature. The brightness of PbSCl is high in comparison to nanosheets, it may be because $PbCl_2$ can act to prevent surface defect, which means reducing dangling bonds and performing as a passivating reagent.

The experimental results shown by Ghadendra B. Bhandari and his co-worker from his paper showed that PbS nanosheet with the same reaction time has a PL peak at 1840±150 nm [59]. There is nearly a 253 nm difference with our sample. It may be because of the difference in reaction time as Bhandari's reaction time was 5 minutes while our reaction time was 20 minutes other reasons may be due to Chlorine ions which may modify the surface energy and increase the growth rate in comparison to his methods, as we are using OLA and $PbCl_2$ instead of 1,1,2-trichloroethane (TCE) for chloroalkane for linking quantum dots while synthesis.

5.3 X-Ray diffraction (XRD)

XRD is one of the best techniques to find the morphology of crystals. Here we will compare our XRD data with standard peaks of PbS (Galena) and $PbCl_2$ because we assume PbSCl nanoplatelets have a core/shell of PbS and $PbCl_2$.

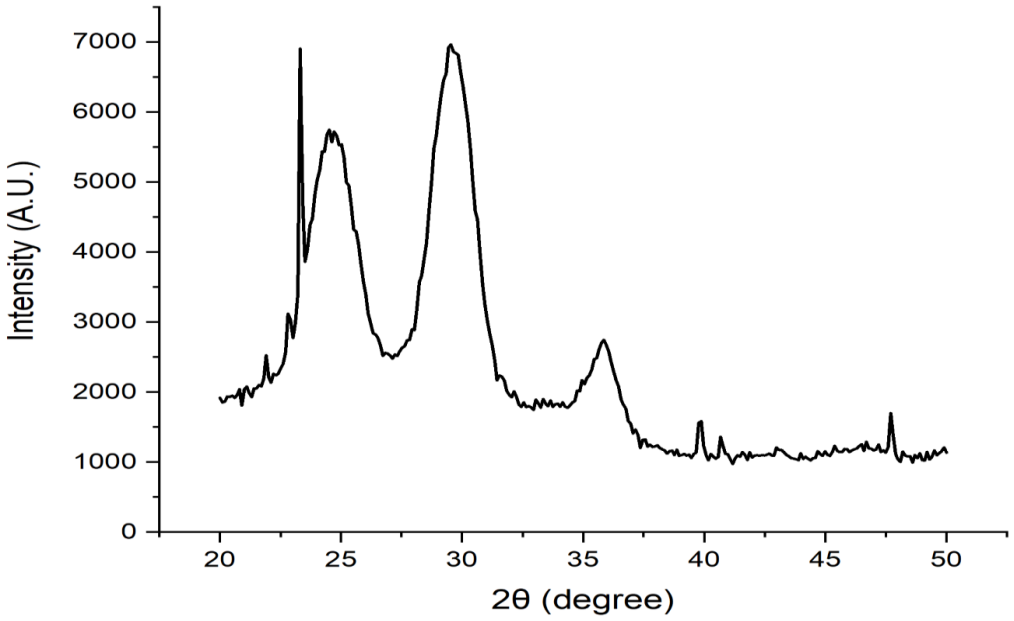

Figure 5.3: XRD of PbSCl nanoplatelets synthesis at 130^0C for 20 minutes.

Table2 is for standard peak and peak obtained from our nanoplatelets sample.

Table 2. Standard peak for PbS (Galena), $PbCl_2$ and PbSCl nanoplatelets.

	PbSCl NPL		Standard peak from web	
Peaks		Facet	$PbCl_2$	PbS
19.61		<200>		
21.89	21.9			
22.84	22.91		22.84	
23.32	23.3	<111>		
24.85	24.8	<201>	24.85	
30.64	29.83	<211>		30.64
32.22	35.85		32.22	
35.22				
37.6				
39.72				
40.71				
41.94				
43.12				43.12

From the above graph, we can see peaks at 24.85^0, 29.83^0, and 35.85^0 shows broader peaks and 19.8^0, 22^0, 23^0, 40^0, and 47^0 show sharper peaks. As we know if the sample shows a favored alignment of crystal planes in a specific direction, then we can see broader diffraction peaks. We saw broader peaks in such specific angles because the X-ray beam interacts more effectively with that aligned plane, causing more pronounced diffraction in those directions. When we use the Scherrer equation, on the above broader peaks angle, the estimated sizes were 5.6 nm, 6.4 nm, and 8.7nm respectively. These are close values as obtained from my colleague

observed from HRTEM. We can see some peaks of PbO are missing, it may be due to the background or dominated by $PbCl_2$ and may appear when we reduce the Cl composition in our synthesis process. The broad peak observed at 24.97^0 is likely attributed to the diffraction of (111) planes of the PbS core. This specific peak is commonly seen in the X-ray diffraction patterns of pure PbS nanoribbons. On the other hand, the peaks observed at 31.35^0 and 35.81^0 are probably originating from $PbCl_2$.

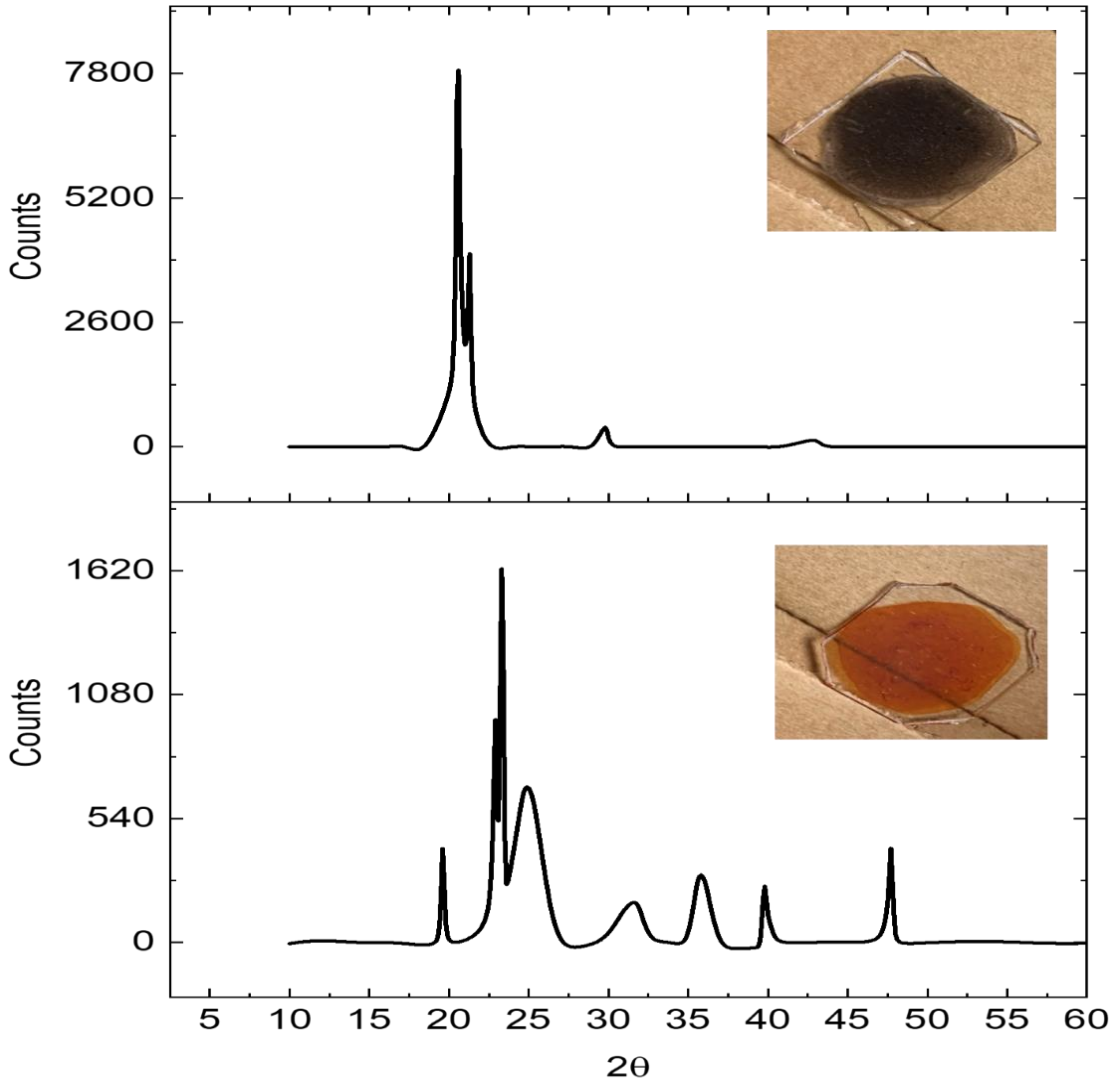

Figure 5.4: XRD of PbS/PbCl core/shell nanoplatelets before (a) and after (b) washed by OLA.

One of my colleagues has demonstrated that the $PbCl_2$ shell can be eliminated by treating the nanoplatelets with OLA. OLA was used to dissolve $PbCl_2$ and prepare lead precursors during the synthesis process. This treatment has the potential to remove the $PbCl_2$ shell and potentially form a PbCl alloy. Following the OLA treatment, the nanoplatelets change from orange nanoplatelets to black color, which is the characteristic color of PbS nanoplatelets. The XRD pattern also reveals the emergence of two peaks at 29^0 and 43^0, corresponding to the (200) and (220) crystal planes of PbS.

5.4 Absolute PL quantum yield measurement

This is one of the characterization processes where we measure the brightness of our sample.

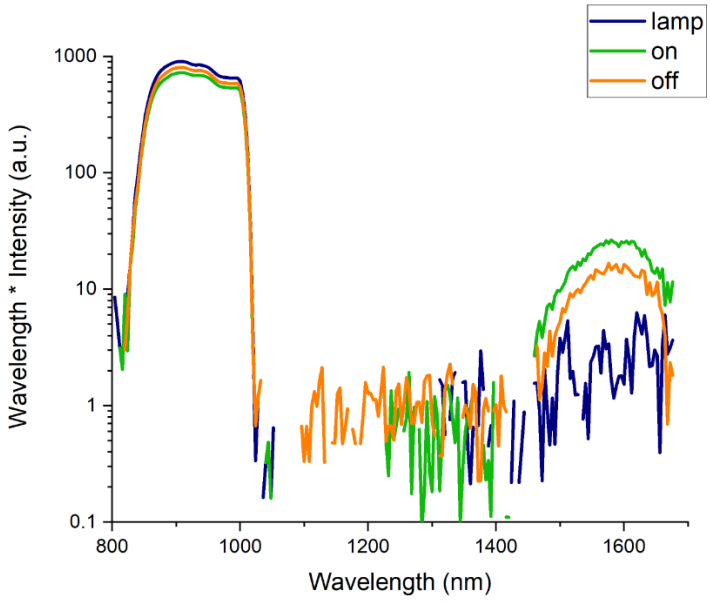

Figure 5.5: Experimental graph of PbSCl nanoplatelets for the measurement of quantum yield.

As we are using Friend et al. methods to calculate quantum yield. The first peak is the excitation peak while the second peak is the PL peak. The excitation was done from the lamp, and emission was measured from it. Blue curves indicate the excitation and PL from the integrating sphere while green and orange are from the sample at on and off positions respectively. Off position means the sample in the cuvette kept inside the integrating sphere but beam of light not colliding directly with it while on position ns the excitation beam collides directly with the simple measurement, we got a quantum yield of 13% with absorption coefficients of 8%. We can compare the quantum yield between PbS nanoparticles, which is shown in the table 3.

Table 3. Quantum yield value for PbS nanoparticles and PbSCl nanoplates.

	PbS nanosheets [16]	PbS nanoribbon [16]	PbSCl nanoplatelets
QY	3.4 %	5.7 %	13%

The quantum yield of PbSCl is double then PbS nanoribbon and nearly four times higher than PbS nanosheets. It may be due to the presence of more surface defects in sheets and ribbons in comparison to the nanoplatelets. We can assume that due to the use of $PbCl_2$ to chain the quantum dots instead of TCA, while doing synthesis may reduce the surface defects or $PbCl_2$ helps to passivate the PbSCl nanoplatelets.

5.5. Time-resolved photoluminescence decay (TPL)

The time-resolved photoluminescence (PL) decay analysis of PbSCl nanoplatelets has revealed a primarily single exponential decay behavior, although in this particular sample, a double exponential decay was observed. Upon comparing the data with PbS nanosheets, it was found that the lifetime of PbSCl nanoplatelets is longer than that of nanosheets and nanoribbons. This extended lifetime can be attributed to the passivation of surface trap sites and a reduction in defects achieved by the process of $PbCl_2$. After conducting double exponential decay fitting using Origin Pro, two-time constants, $\tau_1$and τ_2, were determined as fast component decay constant 304.839 ns and slow component decay constant, 708.220ns respectively. The reduction in surface trap sites and defects due to $PbCl_2$ treatment resulted in a substantial increase in the radiative recombination rate, leading to a longer lifetime of the photoluminescence (PL) signal. The research indicates that PbSCl nanoplatelets exhibit favorable optical properties, with extended PL lifetime, potentially making them promising candidates for various optoelectronic applications. Passivation affects the $PbCl_2$ contribute to the enhanced radiative recombination, further validating the importance of surface engineering in colloidal nanocrystals to optimize their performance in different applications.

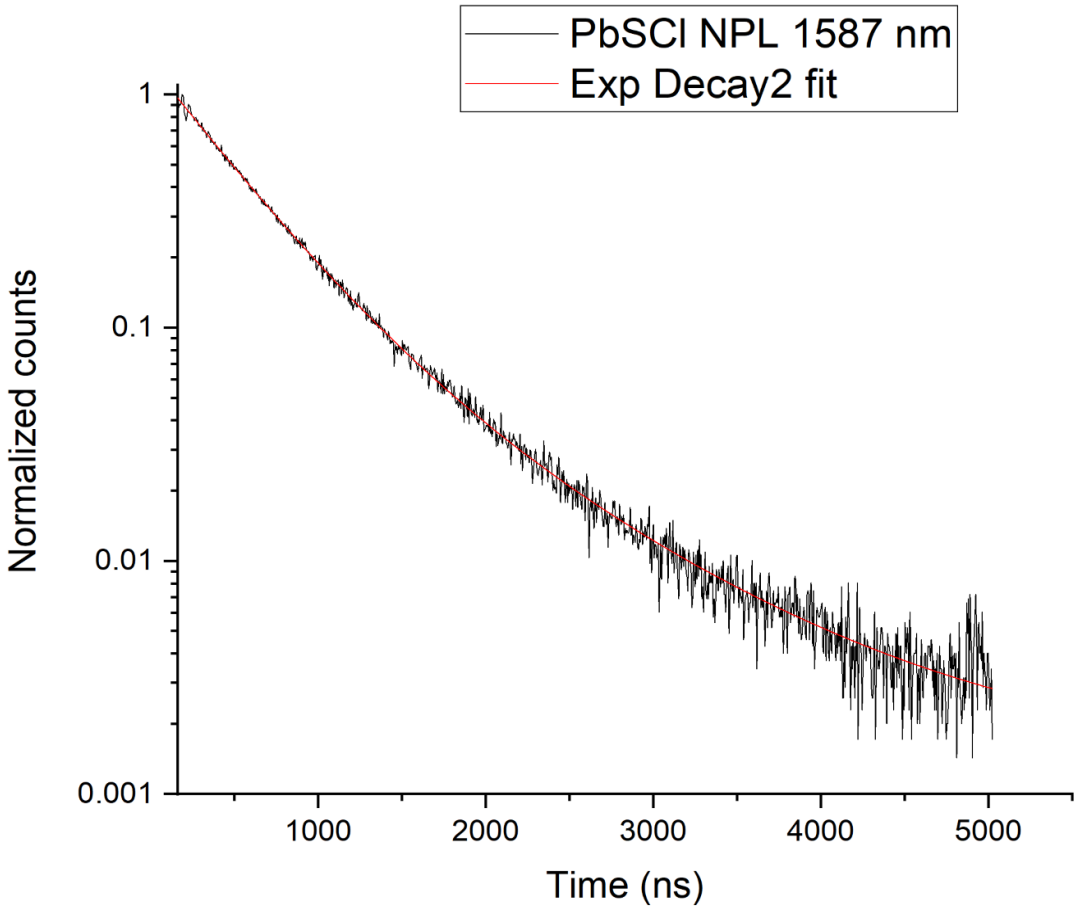

Figure 5.6: TPL measurement of PbSCl nanoplatelets at 1582 nm excited by 532 nm pulse laser.

5.6 Conclusions

To summarize, we have successfully developed a method to synthesized PbS/PbCl2 nanoplatelets by adapting the procedure used for the synthesis of PbS nanosheets, as discussed in chapter 2. Preliminary results indicate that nanoplatelets of varying thickness are formed, with the thickness largely dependent on the degree of degassing and the reaction temperature. This conclusion was confirmed by examining the nanoplatelets trough TEM imaging. The optical properties of the synthesized nanoplatelets are quite promising. With an absolute quantum yield

exceeding 10%, the efficiency of these nanoplatelets is approximately twice that of PbS nanoribbons. This significant increase in quantum yield underscores the potential of these nanoplatelets for optoelectronic applications and emphasizes the effectiveness of our newly developed synthesis method. These findings present an exciting avenue for future research in the quest for optimizing the properties of colloidal nanocrystals for various applications.

5.7 Future work

In this project, our goal was to develop a repeatable synthesis method for nanoplatelets. Most of the optical properties characterizations were carried out on nanoplatelets synthesized at 130^0C for 20 minutes. In the future, we aim to conduct syntheses at various temperatures and measure the thickness of each sample through photoluminescence (PL, TPL, and quantum yield analyses. We are also interested in exploring the potential effects of substituting the linking chlorine with other halogens, such as bromine and Iodine. We have already observed some intriguing properties when we replace $PbCl_2$ with PbI and $PbBr_2$, further validating the potential of these substitutions. Our research continues in this project, with a current focus on detecting amplified spontaneous emission (ASE form our nanoplatelets. Preliminary results have been quite promising. We believe that our ongoing investigations will contribute to the enhancement of nanoplatelet synthesis methods and the understanding of their optical properties, potentially advancing their applications in optoelectronic and related fields.

REFERENCES

[1] G. A. Mansoori, *Principles of Nanotechnology: Molecular-Based Study of Condensed Matter in Small Systems.* 2005.

[2] C. P. Neupane, "No title," *Time Resolved Optical Spectroscopy of Colloidal PbS Nanosheets,* 2018.

[3] S. W. Koch *et al*, "Semiconductor excitons in new light," *Nature Materials,* vol. 5, *(7),* pp. 523-531, 2006.

[4] C. Kittel, *Introduction to Solid State Physics.* 2005.

[5] J. Jiao *et al*, "Synthesis of PbS nanoflowers by biomolecule-assisted method in the presence of supercritical carbon dioxide," *Solid State Sciences,* vol. 11, *(5),* pp. 976-981, 2009.

[6] A. P. Alivisatos, "Semiconductor clusters, nanocrystals, and quantum dots," *Science,* vol. 271, *(5251),* pp. 933-937, 1996.

[7] B. Hyun *et al*, "Electron injection from colloidal PbS quantum dots into titanium dioxide nanoparticles," *ACS Nano,* vol. 2, *(11),* pp. 2206-2212, 2008.

[8] V. González-Pedro *et al*, "High performance PbS Quantum Dot Sensitized Solar Cells exceeding 4% efficiency: the role of metal precursors in the electron injection and charge separation," *Physical Chemistry Chemical Physics,* vol. 15, *(33),* pp. 13835-13843, 2013.

[9] S. Hatami et al, "Absolute photoluminescence quantum yields of IR26 and IR-emissive Cd 1− x Hg x Te and PbS quantum dots–method-and material-inherent challenges," Nanoscale, vol. 7, (1), pp. 133-143, 2015.

[10] L. V. Kulik et al, "Dielectric enhancement of excitons in near-surface quantum wells," Physical Review B, vol. 54, (4), pp. R2335, 1996.

[11] S. G. Tikhodeev et al, "Excitons in near surface quantum wells: Local probe of semiconductor/vacuum surface," Physica Status Solidi (a), vol. 164, (1), pp. 179-182, 1997.

[12] G. Binnig and H. Rohrer, "Scanning tunneling microscopy," Surf. Sci., vol. 126, (1-3), pp. 236-244, 1983.

[13] P. R. Aranda et al, "Nanomaterials in fluorescent laser-based immunosensors: Review and applications," Microchemical Journal, vol. 141, pp. 308-323, 2018.

[14] C. Schliehe et al, "Ultrathin PbS sheets by two-dimensional oriented attachment," Science, vol. 329, (5991), pp. 550-553, 2010.

[15] K. Burke and L. O. Wagner, "DFT in a nutshell," International Journal of Quantum Chemistry, vol. 113, (2), pp. 96-101, 2013.

[16] A. D. Antu et al, "Bright colloidal PbS nanoribbons," Chemistry of Materials, vol. 30, (11), pp. 3697-3703, 2018.

[17] J. Tang et al, "Colloidal-quantum-dot photovoltaics using atomic-ligand passivation," Nature Materials, vol. 10, (10), pp. 765-771, 2011.

[18] J. M. Luther et al, "Schottky solar cells based on colloidal nanocrystal films," Nano Letters, vol. 8, (10), pp. 3488-3492, 2008.

[19] M. V. Kovalenko, M. Scheele and D. V. Talapin, "Colloidal nanocrystals with molecular metal chalcogenide surface ligands," Science, vol. 324, (5933), pp. 1417-1420, 2009.

[20] Q. Wei, Synthesis, Properties and Applications of Nanorods and Nanowires. 2001.

[21] S. Acharya et al, "Shape-dependent confinement in ultrasmall zero-, one-, and two-

dimensional PbS nanostructures," *J. Am. Chem. Soc.,* vol. 131, *(32),* pp. 11282-11283, 2009.

[22] C. R. Oliver *et al*, "Robofurnace: A semi-automated laboratory chemical vapor deposition system for high-throughput nanomaterial synthesis and process discovery," *Rev. Sci. Instrum.,* vol. 84, *(11),* 2013.

[23] H. Zeng *et al*, "Nanomaterials via laser ablation/irradiation in liquid: a review," *Advanced Functional Materials,* vol. 22, *(7),* pp. 1333-1353, 2012.

[24] A. Mignot *et al*, "A Top-Down synthesis route to ultrasmall multifunctional Gd-Based silica nanoparticles for theranostic applications," *Chemistry–A European Journal,* vol. 19, *(19),* pp. 6122-6136, 2013.

[25] H. Zhang et al, "Colloidal synthesis of PbS and PbS/CdS nanosheets using acetate-free precursors," Chemistry of Materials, vol. 28, (1), pp. 127-134, 2016.

[26] S. M. Premathilaka et al, "A robust method for the synthesis of colloidal PbS nanosheets," Physica Status Solidi (RRL)–Rapid Research Letters, vol. 10, (11), pp. 838-842, 2016.

[27] M. A. Hines and G. D. Scholes, "Colloidal PbS nanocrystals with size-tunable near-infrared emission: observation of post-synthesis self-narrowing of the particle size distribution," Adv Mater, vol. 15, (21), pp. 1844-1849, 2003.

[28] P. Scherrer, "Bestimmung der Grosse und inneren Struktur von Kolloidteilchen mittels Rontgenstrahlen," Nach Ges Wiss Gottingen, vol. 2, pp. 8-100, 1918.

[29] Photoluminescence explained [Internet]; c2023 [cited 2023 07/.23]. Available from: http://www.renishaw.com/en/photoluminescence-explained--25809.

[30] S. Chiluwal, "No title," Understanding the Growth Mechanism of Pbse Nanorods, 2016.

[31] S. Khan, "Colloidai PbS and PbS/CdS nanosheets heterostructure," Bowling Green State

University, 2015.

[32] J. C. de Mello, H. F. Wittmann and R. H. Friend, "An improved experimental determination of external photoluminescence quantum efficiency," *Adv Mater,* vol. 9, *(3),* pp. 230-232, 1997.

[33] T. J. Wenzel, "No title," Douglas A.Skoog, Donald M.West, F.James Holler, and Stanley R.Crouch: Fundamentals of Analytical Chemistry, International Ed., 2013.

[34] A. D. Antu, "No title," Morphology and Surface Passivation of Colloidal PbS Nanoribbons, 2017.

[35] T. A. Driscoll et al, "Efficient second-harmonic generation in KTP crystals," Josa B, vol. 3, (5), pp. 683-686, 1986.

[36] J. R. Lakowicz, Principles of Fluorescence Spectroscopy. 2006.

[37] A. A. Bakulin et al, "Charge trapping dynamics in PbS colloidal quantum dot photovoltaic devices," Acs Nano, vol. 7, (10), pp. 8771-8779, 2013.

[38] K. S. Jeong et al, "Enhanced mobility-lifetime products in PbS colloidal quantum dot photovoltaics," ACS Nano, vol. 6, (1), pp. 89-99, 2012.

[39] K. Szendrei et al, "PbS nanocrystal solar cells with high efficiency and fill factor," Appl. Phys. Lett., vol. 97, (20), 2010.

[40] M. J. Fernee et al, "Inorganic surface passivation of PbS nanocrystals resulting in strong photoluminescent emission," Nanotechnology, vol. 14, (9), pp. 991, 2003.

[41] X. Huang, E. Lindgren and J. R. Chelikowsky, "Surface passivation method for semiconductor nanostructures," Physical Review B, vol. 71, (16), pp. 165328, 2005.

[42] G. K. Grandhi and R. Viswanatha, "Understanding the role of surface capping ligands in passivating the quantum dots using copper dopants as internal sensor," *The Journal of Physical Chemistry C,* vol. 120, *(35),* pp. 19785-19795, 2016.

[43] M. A. Boles *et al*, "The surface science of nanocrystals," *Nature Materials,* vol. 15, *(2),* pp. 141-153, 2016.

[44] C. Pu *et al*, "Electrochemically-stable ligands bridge the photoluminescence-electroluminescence gap of quantum dots," *Nature Communications,* vol. 11, *(1),* pp. 937, 2020.

[45] A. H. Khan *et al*, "Near-Infrared emitting colloidal PbS nanoplatelets: lateral size control and optical spectroscopy," *Chemistry of Materials,* vol. 29, *(7),* pp. 2883-2889, 2017.

[46] E. Lhuillier *et al*, "Electrolyte-gated colloidal nanoplatelets-based phototransistor and its use for bicolor detection," *Nano Letters,* vol. 14, *(5),* pp. 2715-2719, 2014.

[47] Z. Chen *et al*, "Quasi-2D colloidal semiconductor nanoplatelets for narrow electroluminescence," *Advanced Functional Materials,* vol. 24, *(3),* pp. 295-302, 2014.

[48] M. Lorenzon *et al*, "Reversed oxygen sensing using colloidal quantum wells towards highly emissive photoresponsive varnishes," *Nature Communications,* vol. 6, *(1),* pp. 6434, 2015.

[49] B. Guzelturk *et al*, "Amplified spontaneous emission and lasing in colloidal nanoplatelets," *ACS Nano,* vol. 8, *(7),* pp. 6599-6605, 2014.

[50] C. She et al, "Low-threshold stimulated emission using colloidal quantum wells," Nano Letters, vol. 14, (5), pp. 2772-2777, 2014.

[51] J. Q. Grim et al, "Continuous-wave biexciton lasing at room temperature using solution-processed quantum wells," Nature Nanotechnology, vol. 9, (11), pp. 891-895, 2014.

[52] A. Naeem et al, "Giant exciton oscillator strength and radiatively limited dephasing in two-dimensional platelets," Physical Review B, vol. 91, (12), pp. 121302, 2015.

[53] E. Lhuillier et al, "Two-dimensional colloidal metal chalcogenides semiconductors: synthesis, spectroscopy, and applications," Acc. Chem. Res., vol. 48, (1), pp. 22-30, 2015.

[54] M. D. Tessier et al, "Spectroscopy of single CdSe nanoplatelets," ACS Nano, vol. 6, (8), pp. 6751-6758, 2012.

[55] J. Yu and R. Chen, "Optical properties and applications of two-dimensional CdSe nanoplatelets," InfoMat, vol. 2, (5), pp. 905-927, 2020.

[56] M. D. Tessier et al, "Spectroscopy of colloidal semiconductor core/shell nanoplatelets with high quantum yield," Nano Letters, vol. 13, (7), pp. 3321-3328, 2013.

[57] A. Dey et al, "State of the art and prospects for halide perovskite nanocrystals," ACS Nano, vol. 15, (7), pp. 10775-10981, 2021.

[58] S. V. Firstov *et al*, "Compact and efficient O-band bismuth-doped phosphosilicate fiber amplifier for fiber-optic communications," *Scientific Reports,* vol. 10, *(1),* pp. 11347, 2020.

[59] G. B. Bhandari *et al*, "Thickness-controlled synthesis of colloidal PbS nanosheets and their thickness-dependent energy gaps," *Chemistry of Materials,* vol. 26, *(19),* pp. 5433-5436, 2014.

[60] G. M. Akselrod *et al*, "Efficient nanosecond photoluminescence from infrared PbS quantum dots coupled to plasmonic nanoantennas," *Acs Photonics,* vol. 3, *(10),* pp. 1741-1746, 2016.

[61] S. Brittman *et al*, "Effects of a lead chloride shell on lead sulfide quantum dots," *The Journal of Physical Chemistry Letters,* vol. 10, *(8),* pp. 1914-1918, 2019.

[62] P. B. Green *et al*, "PbS nanocrystals made using excess lead chloride have a halide-perovskite-like surface," *Chemistry of Materials,* vol. 33, *(23),* pp. 9270-9284, 2021.

[63] S. W. Winslow *et al*, "Quantification of a PbCl x Shell on the Surface of PbS Nanocrystals," *ACS Materials Letters,* vol. 1, *(2),* pp. 209-216, 2019.